UPCommons

Portal del coneixement obert de la UPC

http://upcommons.upc.edu/e-prints

On the evolution of flow topology in turbulent Rayleigh-Bénard convection

F.Dabbagh,[1, a)] F.X.Trias,[1, b)] A.Gorobets,[1, 2, c)] and A.Oliva[1, d)]

[1)]*Heat and Mass Transfer Technological Centre, Technical University of Catalonia, ETSEIAT, c/Colom 11, 08222 Terrassa, Spain*

[2)]*Keldysh Institute of Applied Mathematics, 4A, Miusskaya Sq., Moscow 125047, Russia*

(Dated: 28 October 2016)

Small-scale dynamics is the spirit of turbulence physics. It implicates many attributes of flow topology evolution, coherent structures, hairpin vorticity dynamics and mechanism of the kinetic energy cascade. In this work, several dynamical aspects of the small scale motions have been numerically studied in a framework of Rayleigh-Bénard convection (RBC). To do so, direct numerical simulations have been carried out at two Rayleigh numbers $Ra = 10^8$ and 10^{10}, inside an air-filled rectangular cell of aspect ratio unity and π span-wise open-ended distance. As a main feature, the average rate of the invariants of the velocity gradient tensor $(Q_{\mathsf{G}}, R_{\mathsf{G}})$ have displayed the so-called "teardrop" spiraling shape through the bulk region. Therein, the mean trajectories are swirling inwards revealing a periodic spin around the converging origin, of a constant period that is found to be proportional to the plumes lifetime. This suggests that the thermal plumes participate in the coherent large-scale circulation and the turbulent wind created in the bulk. Particularly, it happens when the plumes elongate substantially to contribute to the large-scale eddies at the lower turbulent state. Supplementary small-scale properties, which are widely common in many turbulent flows have been observed in RBC. For example, the strong preferential alignment of vorticity with the intermediate eigenstrain vector, and the asymmetric alignment between vorticity and the vortex-stretching vector. It has been deduced that in a hard turbulent flow regime, local self-amplifications of straining regions aid in contracting the vorticity worms, and enhance the local interactions vorticity/strain to support the linear vortex-stretching contributions. On the other hand, the evolution of invariants pertained to the traceless part of velocity-times-temperature gradient tensor have also been considered in order to determine the role of thermals in the fine-scale dynamics. These new invariants show an incorporation of kinetic and thermal gradient dynamics that indicate directly the evolution and lifetime of thermal plumes structures. By applying an identical approach, the rates of the new invariants have shown a symmetric cycling behaviour decaying towards two skew-symmetric converging origins at the lower Ra number. The trajectories near origins address the hot and cold coherent plumes that travel as an average large-scale heat flux in the sidewall vicinities, and denote a periodic spin period close to the plumes lifetime. At the hard turbulent case, the spiraling trajectories travel in shorter tracks to reveal the reduced lifetime of plumes under the dissipative and mixing effects. The turbu-

lent background kinetic derivatives get self amplified and the trajectories converge to a zero-valued origin indicating that there is no contribution from the plumes to the average coherent large scales of heat flux. These and other peculiar scrutinies on the small scale motions in RBC have been enlightened, and may have a fruitful consequence on modelling approaches of buoyancy-driven turbulence.

a) firas@cttc.upc.edu

b) xavi@cttc.upc.edu

c) andrey@cttc.upc.edu

d) oliva@cttc.upc.edu

I. INTRODUCTION

"Turbulent flow constitutes an unusual and difficult problem of statistical mechanics, characterized by extreme statistical disequilibrium, by anomalous transport processes, by strong dynamical nonlinearity, and by perplexing interplay of chaos and order" (Kraichnan[1]). Nevertheless, understanding the qualitative contents of the governing equations of turbulence can elucidate many physics therein. Namely, generic structural properties of the mathematical governing objects, called (strange) attractors, which are invariants in some sense, include many ingredients of turbulence physics (Tsinober[2]). Hence, the key point is in the small scale motions, and their universal qualitative aspects commonly found in a wide variety of turbulent flows. They result from the subtle balance between convective transport and diffusive dissipation to be definitely blameworthy of generating the hairpin vorticity dynamics, non-Gaussianity, strain/dissipation production and the cascade of kinetic energy mechanisms. Studying their evolution gives us fundamental perspectives of flow topology and thus, many physics of turbulence become intelligible.

Since the early 90s, a major attention has been given to the important role of velocity derivatives in the topological classification of fluid motions[3] and the small-scale dynamics[4,5]. Thereby, several universal features of the small scale turbulence are observed, *e.g.* the inclined "teardrop" shape of the joint probability density function (PDF) of Q_{G} (the second) and R_{G} (the third) invariants of the velocity gradient tensor, and the essential preferential alignment of vorticity with the intermediate eigenvector of the rate-of-strain tensor. They have been observed in various turbulent flow configurations such as isotropic turbulence[5], turbulent boundary layer[6], channel flow[7], turbulent mixing layer[8] and turbulent jets[9]. However, their thermally driven analogues, as in the developed natural convection flow heated from below and cooled from above, namely Rayleigh-Bénard convection (RBC), are far from being satisfactory.

Buoyancy-driven flow in RBC has always been an important subject of scientific studies with numerous applications in environment and technology. It constitutes a canonical flow that approaches many natural and industrial processes such as ventilation of indoor spaces, cooling of electronic devices and coherent circulations in solar collectors, oceans

and atmosphere. In spite of its well-defined mathematical formulae, in principle given by Navier-Stokes (NS)–under Boussinesq approximation–and energy equations (see Section II), the resultant dynamics is strongly featured by intrinsic instabilities, counter-gradient diffusion, augmented pressure fluctuations and strong interactions between kinetics and thermals diversely distributed over flow regions. This nature has inspired significant inherent complexities in the view of turbulence models, and the proper reproduction to the coherent large-scale circulations in RBC[11]. Therefore, understanding the dynamics of small scale motions and their lifetime evolution can play a major role in the scope of turbulence modeling. Indeed, a considerable advancement that unravels many involved physics of the problem has been obtained across theories[12,13], experiments and numerical studies (see Chilla and Schumacher[14] as an overall recent reference). The small-scale properties were a focal point for many authors, *e.g.* Lohse and Xia[15], who investigated the so-called Bolgiano-Obukhov scaling existence within RBC. Moreover, the direct numerical simulation (DNS) of Schumacher[16] and experiments of Gasteuil *et al.*[17] have monitored the turbulent local evolution of the thermal plumes in a Lagrangian frame to explore important statistical aspects of heat and momentum transport mechanisms. Some authors focused on studying the substantial turbulent components of thermal and kinetic energy dissipation rates, which tightly collaborate with high fluctuations and small-scale intermittency[18,19]. Only Schumacher *et al.*[20] have recently shed light on the universality picture of small scales in RBC regarding their scaling law performance. Even more recently, Park and Lee[10] have addressed a new study of the coherent structures in RBC using the joint PDF of the velocity gradient tensor. Their analysis[10] is limited to a soft turbulence regime, and no descriptions on the universal features of the small scale motions, the mechanisms of their dynamics and flow topology changes are given.

In this study, we provide an investigation on the dynamical universal features of small scale motions in RBC, commonly observed in many turbulent flows. Basically, the average evolution of Q_{G} and R_{G} invariants (defined in Section III) of velocity gradient tensor $\mathsf{G} = \nabla \boldsymbol{u}$, is studied within the bulk region to show the cyclical action of flow topology change converging towards the origin. By doing so, we extend the averaging dynamical approach applied to isotropic turbulence[4,5] and a turbulent boundary layer (BL)[6], to include the topology dynamics of RBC through the bulk. Important insights concerning the dynamics

5

at hard turbulent regime, and the characteristic lifetime of the coherent energy containing eddies are explored, where the universal essential alignments of vorticity with straining and vortex-stretching geometries are addressed. On the other hand, an identical approach is considered for the novel invariants $Q_{\tilde{\mathsf{G}}_\theta}$ and $R_{\tilde{\mathsf{G}}_\theta}$ (defined in Section IV) of the traceless part of the velocity-times-temperature gradient tensor $\tilde{\mathsf{G}}_\theta = \nabla(\boldsymbol{u}T) - 1/3tr(\nabla(\boldsymbol{u}T))\mathsf{I}$. The new invariants are introduced as combinations of thermal and kinetic small-scale topology and related predominantly with the dynamics of thermal plumes and turbulent heat flux. The new dynamical equations are deduced and the material averaging procedure is applied in order to provide new aspects of the life cycle of the small scales pertained to the thermals, which become worthwhile in turbulence modeling of RBC.

The remainder of the paper is organized as follows. Details over the DNS study in the current configurations of RBC are introduced in Section II. The universal features of fine-scale dynamics and flow topology are discussed by analysing the averaged evolution of the classical velocity gradient tensor invariants in Section III. The pioneering invariants of the new velocity-times-temperature gradient tensor are considered and analysed identically in Section IV. Finally, conclusions and future remarks are reported.

II.   DETAILS OF THE DIRECT NUMERICAL SIMULATION

The data set used in this work is based on instantaneous fields of a DNS study in a Rayleigh-Bénard framework. Namely, we simulate the incompressible NS and thermal energy equations given by:

$$\frac{D\boldsymbol{u}}{Dt} = \sqrt{\frac{Pr}{Ra}}\nabla^2\boldsymbol{u} - \nabla p + \boldsymbol{f}, \qquad \nabla \cdot \boldsymbol{u} = 0, \tag{1}$$

$$\frac{DT}{Dt} = \frac{1}{\sqrt{RaPr}}\nabla^2 T, \tag{2}$$

where $D/Dt = \partial/\partial t + (\boldsymbol{u} \cdot \nabla)$ is the Lagrangian derivative, p is the pressure, T is the temperature and $\boldsymbol{u} = (u, v, w)$ is the velocity vector in Cartesian coordinates $\boldsymbol{x} = (x, y, z)$. Equations (1) and (2) are written in a non-dimensional form using the height of the fluid layer H, the temperature difference between the upper and the lower surfaces $\Delta\Theta$ and the free-fall velocity $U_{ref} = (\alpha g \Delta\Theta H)^{1/2}$ as references, where α is the volumetric thermal expansion coefficient and g is the gravitational acceleration. Namely, U_{ref}, ρU_{ref}^2, $\Delta\Theta$ and H/U_{ref} are

6

used as characteristic scales for $\boldsymbol{u}$, p, T and the time t respectively, where ρ is the fluid density. $\boldsymbol{f} = (0, 0, T)$ indicates the body force vector using the Boussinesq approximation. The current configurations are translated through a squared cross-section cavity of aspect ratio $\Gamma = W/H = 1$ and longitudinal spanwise open-ended distance $L/H = \pi$ (see Figure 1). No-slip boundary conditions for velocity are imposed at the four solid walls. Regarding temperature, the vertical walls are adiabatic, *i.e.* $\partial T / \partial y = 0$, and the horizontal walls are subjected to uniform dimensionless temperatures $T_{hot} = 0.5$ and $T_{cold} = -0.5$ at the bottom and the top walls, respectively. Periodic boundary conditions are applied for all quantities in the longitudinal x-direction. The characteristic parameters of the system are introduced
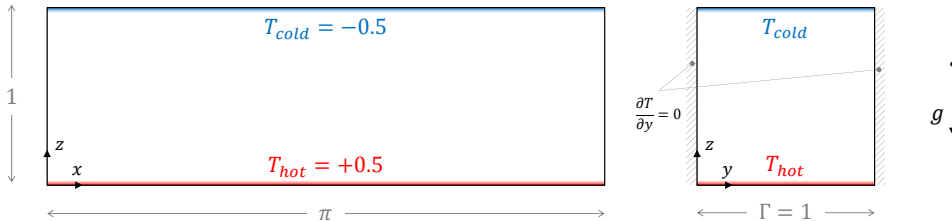

FIG. 1: Schematic representation of the studied Rayleigh-Bénard convective cell.

within the numbers of Prandtl $Pr = \nu/\kappa$ (here $Pr = 0.7$) and Rayleigh $Ra = g\alpha\Delta\Theta H^3/\nu\kappa$ (10^8 and 10^{10}), and in responding to that physics, the average Nusselt number Nu is given by:

$$Nu = \sqrt{RaPr}\langle wT \rangle_A - \frac{\partial \langle T \rangle_A}{\partial z}, \tag{3}$$

where the angular brackets operator $\langle \cdot \rangle$ indicates the temporal average (likewise it denotes the ensemble average in the statistical analysis), and the subscript symbol A refers to the average over $(x\text{-}y)$ plane at position z. ν is the kinematic viscosity and κ is the thermal diffusivity.

Numerically, the governing equations (Eqs.1 and 2) are discretised in space on a Cartesian staggered grid using a finite-volume fourth-order symmetry-preserving scheme[21] that preserves the underlying symmetry properties of the continuous differential operators. Following an operator-based formulation, the discretised NS equations (Eq.1) are given by:

$$\boldsymbol{\Omega}\frac{d\boldsymbol{u}_h}{dt} = -\mathbf{C}(\boldsymbol{u}_h) + \mathbf{D}\boldsymbol{u}_h - \mathbf{M}^t\boldsymbol{p}_h + \boldsymbol{f}_h, \qquad \mathbf{M}\boldsymbol{u}_h = \mathbf{0}_h, \tag{4}$$

where $\boldsymbol{u}_h$ is the discrete velocity vector, $\mathbf{M}$ is the discrete divergence operator and $\boldsymbol{\Omega}$ is a

diagonal matrix, which contains the sizes of the control volumes. The resulting convective coefficient matrix, $\mathbf{C}(\boldsymbol{u}_h)$, is skew-symmetric and the discrete diffusive operator, $\mathbf{D}$, is a symmetric negative-definite matrix. These global discretization properties ensure both the stability and that the global kinetic-energy balance is exactly satisfied even for coarse meshes. Therefore, the kinetic energy is not systematically damped by the discrete convective term, or does not need to be damped explicitly to ensure stability of the method. Regarding the time evolution of the cell-centered temperature, T_h, it is discretised in the same way. Then, for the temporal discretization, a second-order self-adapting explicit scheme is used[22]. Unlike the conventional explicit integration schemes, it is not based on a standard Courant-Friedrichs-Lewy (CFL) condition. Instead, the eigenvalues of the dynamical system are analytically bounded, and the linear stability domain of the time-integration scheme is adapted in order to maximize the time step, Δt. More details can be found in Trias *et al.*[22]. Finally, the velocity-pressure coupling is then solved by means of a classical fractional step projection method[23]: a predictor velocity $\boldsymbol{u}_h^p$ is explicitly evaluated without considering the contribution of the pressure gradient. Then, imposing the incompressibility constraint, $\mathbf{M}\boldsymbol{u}_h^{n+1} = \mathbf{0}_h$, leads to a Poisson equation for $\boldsymbol{p}_h^{n+1}$ to be solved at each time step using the Fourier-based solver[24]. Briefly, it is a scalable parallel solver that uses diagonalization by means of a FFT in the periodic direction to uncouple the original 3D system into a set of independent 2D systems. These 2D systems are solved using a preconditioned conjugate gradient method except for the first lowest-frequency systems which are problematic for an iterative solver. Those few systems are solved with a parallel direct Schur complement-based method. The accuracy of the solution is automatically tuned during simulation in order to provide the requested reduction of the divergence norm $|\mathbf{M}\boldsymbol{u}_h^{n+1}|/|\mathbf{M}\boldsymbol{u}_h^p| \leqslant 10^{-3}$ on each time step. Finally, the absolute value of the resulting divergence norm is attained to 10^{-10}. The grids are constructed with a uniform grid spacing in the periodic x-direction, while the wall-normal points are distributed following a hyperbolic-tangent function with an equal number of nodes ($N_y = N_z$), given in z-direction (identical for y-direction) by

$$z_i = \frac{1}{2}\left(1 + \frac{\tanh\{\gamma_z(2(i-1)/N_z - 1)\}}{\tanh \gamma_z}\right), \qquad i = 1, \ldots, N_z + 1, \tag{5}$$

where γ_z is the concentration factor in the z-direction. For details about the numerical methods, algorithms and verification of the DNS code the reader is referred to Trias *et al.*[25]. RBC is normally identified with predominant thermal and kinetic dissipative small scales

8

which are distributed differentially in the near-walls and the bulk regions[26]. This has always been an important demand to resolve both areas well in order to properly characterize the flow dynamics. To do so, a refinement approach based on the Grötzbach estimate[27] for the Kolmogorov scales, which is given by:

$$\eta_{Gr\ddot{o}} \leq \frac{\pi \, Pr^{1/2}}{((Nu - 1)Ra)^{1/4}} \quad \text{for} \quad Pr \leq 1, \tag{6}$$

has been considered firstly for the low Ra number. By introducing Δz_{max} as the maximum grid spacing applied in the core where $\Delta z_{max} = \Delta y_{max} = \Delta x$, various refinement ratios of the Grötzbach criterion defined as $\Delta z_{max}/\eta_{Gr\ddot{o}} \in [1.1 \rightarrow 0.7]$, have been tested[28]. Furthermore, an investigation has been performed in order to reduce the computational cost by maximizing the equidistant spacing in the periodic x-direction (instead of setting it to $\Delta x = \Delta z_{max}$), at the same Ra number. The numerical tests in this regard have led to a refinement ratio of $\Delta z_{max}/\eta_{Gr\ddot{o}} = 0.9$, and a coarsening tolerance for the homogeneous cell spacing in the range $\Delta x/\Delta z_{max} \in [1.25 \rightarrow 1.5]$, without losing accuracy. These results have later been used to choose the proper estimated grid at $Ra = 10^{10}$ (see table I). On the other hand, the BLs are resolved with $N_{BL} = 9$ and 12 grid points for $Ra = 10^8$ and 10^{10}, respectively. This exceeds the resolution requirements proposed by Shishkina et $al.$[29] and given, for $Pr \approx 0.7$, by:

$$N_{th.BL} \approx 0.35 Ra^{0.15}, \qquad 10^6 \leq Ra \leq 10^{10}, \tag{7}$$

$$N_{v.BL} \approx 0.31 Ra^{0.15}, \qquad 10^6 \leq Ra \leq 10^{10}, \tag{8}$$

where $N_{th.BL}$ and $N_{v,BL}$ are the minimum required number of nodes within the thermal and viscous BLs, respectively.

Data for the current statistical analysis is collected after at least 500 non-dimensional time units $[TU]$ in order to be sure that the statistically steady state is reached and the flow becomes out of the initial transient effects. Temporal integrations are then started and continue during a sufficiently long time, $\tau = 500[TU]$ and $200[TU]$, for the low and high Ra numbers, respectively. They guarantee a statistically stable turbulent heat transport unchanged due to the presence of large-scale circulations, which erratically reverse their directions over many large eddy turnover times[30–32]. In this case, the large eddy turnover lasts about $\tau_{eddy} \sim 7[TU]$ ($Ra = 10^8$) and $5[TU]$ ($Ra = 10^{10}$). It has been defined as $\tau_{eddy} = H/\boldsymbol{u}_{rms}$, where $\boldsymbol{u}_{rms}$ the root mean square of the bulk velocity. The instantaneous

characteristics used in the statistical calculations are collected typically over several large eddy turnover times, τ_{st} (see Table I), which sufficiently ensure the statistics convergence. The bulk region considered in this paper is identified far enough from the solid boundaries and the near-wall influences. Consequently, a subvolume $V_{bulk} = \{\boldsymbol{x} = (x, y, z) | 0.2 \leq y \leq 0.8; 0.2 \leq z \leq 0.8\}$, has been chosen as a representative domain of the bulk, which lays excessively out of the thermal BLs (see Figures 2a and 2b). In order to verify our selection, the vertical midwidth profiles of the x-average root-mean-square temperatures are plotted and displayed in Figure 2a for both cases. The profiles show maximum values at the outlets of the thermal BLs to determine their thickness δ_T at the maximal thermal fluctuation[33]. The corresponding distances read, $z = 0.016$ in the case of $Ra = 10^8$ and $z = 0.0039$ for $Ra = 10^{10}$, which match very well with the theoretical prediction of Grossmann and Lohse[13] that reads $\delta_T = 0.5H/Nu$ ($\delta_T^{Ra=10^8} = 0.0162, \delta_T^{Ra=10^{10}} = 0.0039032$).

All simulation parameters and grid details are displayed in Table I together with the

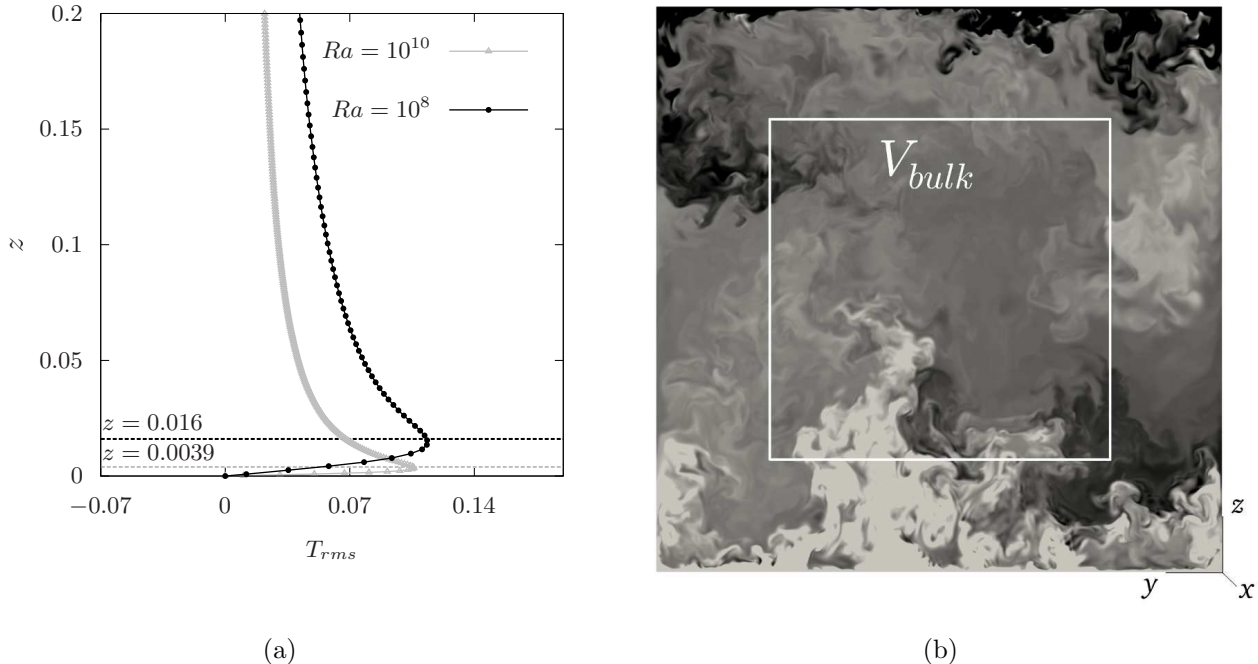FIG. 2: (a) Vertical midwidth and x-average profiles of T_{rms} showed in a closer view due to symmetry. (b) represents an instantaneous temperature in (y, z) plane extracted from the DNS at $Ra = 10^{10}$.

Nu number, which propose a scaling power equal to $\beta \approx 0.309$ in the Ra-function correlation $Nu \sim Ra^\beta$. This value corresponds very well to $\beta = 0.29$ proposed by Grossmann

TABLE I: Summary of simulation parameters with the average Nu results where

$$\eta_{DNS} = (\Delta x \Delta y_{max} \Delta z_{max})^{1/3}.$$

Ra	$\eta_{Grö}$	$\frac{\Delta z_{max}}{\eta_{Grö}}$	$\frac{\Delta x}{\Delta z_{max}}$	η_{DNS}	$\gamma_z = \gamma_y$	$N_x \times N_y \times N_z$	N_{BL}	$\Delta t[TU]$	$\tau[TU]$	$\tau_{st}[\tau_{eddy}]$	Nu
10^8	1.09×10^{-2}	0.70	1.0	7.70×10^{-3}	1.4	$400 \times 208 \times 208$	9	1.45×10^{-3}	500	40	30.9
10^{10}	2.46×10^{-3}	0.92	1.36	2.50×10^{-3}	1.6	$1024 \times 768 \times 768$	12	4.14×10^{-4}	200	10	128.1

and Lohse theory[13] for $Pr \approx 1$ and Ra up to 10^{11}. Moreover, it also agrees with the DNS results of Scheel et al.[34] obtained in a cylindrical cell of aspect ratio unity with the same parameters ($Pr = 0.7$ and $Ra \in [3 \times 10^5 \to 10^{10}]$), and the suggested correlation $Nu = (0.15 \pm 0.01) \times Ra^{0.29 \pm 0.01}$.

(a)

(b)

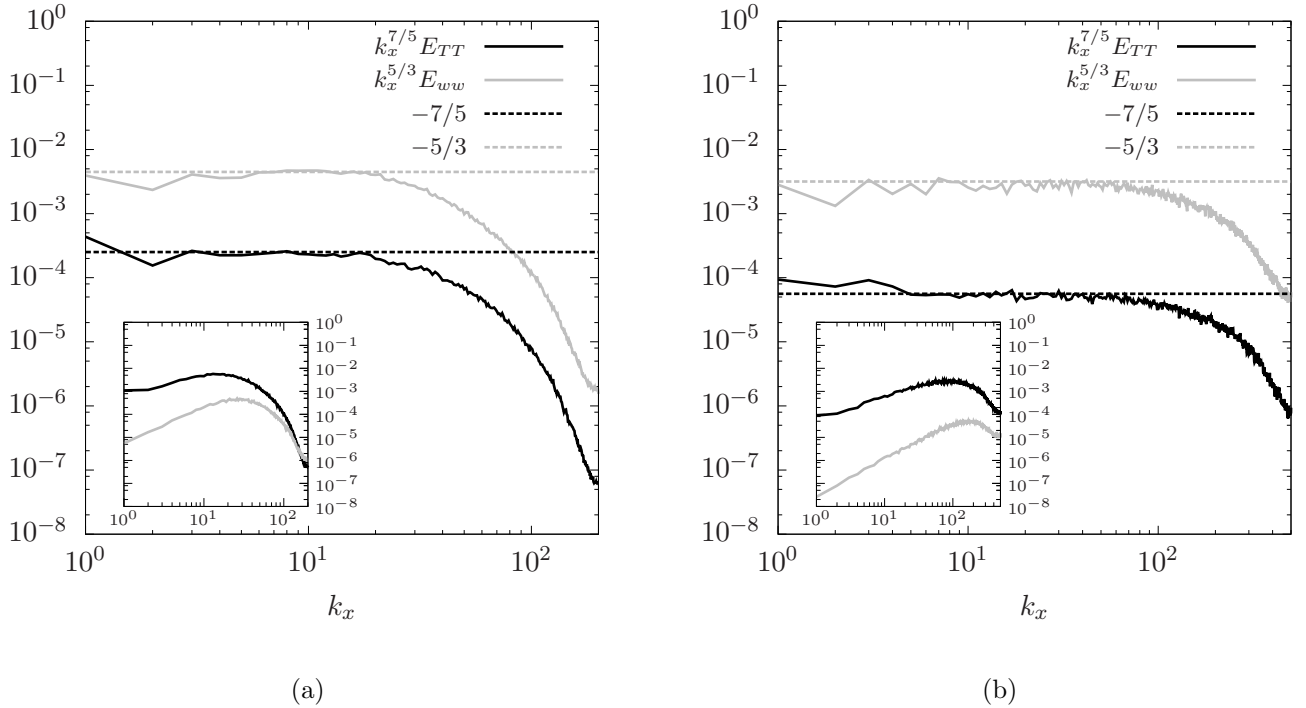FIG. 3: One-dimensional energy spectra in compensated formulae for the vertical velocity $k_x^{5/3} E_{ww}(k_x)$ and the temperature $k_x^{7/5} E_{TT}(k_x)$, extracted along the midwidth periodic x-direction in the core ($z = 0.5$) and inside the thermal BL (insets) at (a) $Ra = 10^8$ and (b) $Ra = 10^{10}$.

Further demonstrations on the solution adequacy can be noted in the collapse of the kinetic

and thermal energy spectra showed in Figure 3. It shows the compensated energy spectra in the periodic x-direction for T and w, taken within the thermal BL (insets) and the core ($z = 0.5$) midway between the lateral walls ($y = 0.5$), and averaged in time. In agreement with many studies, *e.g.* Kaczorowiski and Wagner[33], the velocity and temperature spectra in the centre of the cell correctly match the Kolmogorov $-5/3$ and the Bolgiano $-7/5$ exponents, respectively across the inertial subrange. Hence, all the relevant turbulent scales are resolved by the grids used, and both the inertial subrange and the dissipation range are clearly identified for both turbulent cases in the main sets of Figures 3a and 3b.

Thermal plumes (mushroom-like) have an intrinsic role in activating the energy transport mechanism through the bulk in RBC. In few words, the hot and cold plumes detach respectively from the lower and upper plates. They arise in the bulk with the buoyant acceleration to eventually expand away transforming their portable thermal energy into kinetic one and feeding the momentum[33]. Accordingly to that, and as can be seen in Figure 3, the behaviour of the thermal and kinetic energy spectra in the bulk appears to be opposite to that in the BL. The kinetic energy is placed higher than the thermal spectrum in the core, while it is lower in the BL, as displayed in the insets. On the other hand, the horizontal walls tends to damp the vertical kinetic energy in the near-wall vicinities, and make the scaling exponents in the BL, different (smaller) than in the bulk. Analysis of the spectra at different distances from the horizontal walls[28,33], shows that the level of the kinetic energy is continuously increasing towards the cell centre, while the temperature spectrum is slowly decreasing outside the BL towards the core. That mechanism is basically related to the thermal plumes evolution. Taking a closer view, the thermal energy at $Ra = 10^8$ is higher than its counterpart at $Ra = 10^{10}$ for the lowest wave-number ($k_x^{7/5} E_{TT}(k_x) > 10^{-4}$). This supports the idea that less shedding (conversion into kinetic energy) on thermals takes place for $Ra = 10^8$. The plumes (mushroom-like) are developing farther into the bulk and survive longer in comparison with the case of $Ra = 10^{10}$. This dynamics is familiar in the research studies of RBC, since many have confirmed the decreasing role of thermals, and the reduced characteristic length scales when the Ra number is increased[33].

III. INVARIANTS OF THE CLASSICAL VELOCITY GRADIENT TENSOR

Extensive background material concerning the crucial role of velocity gradients in the topological classification of the flow and small-scale dynamics can be found in many works, e.g. Chong et al.[3], Cantwell et al.[35], Blackburn et al.[7], Soria et al.[8], Perry and Chong[36], Martín et al.[4], Ooi et al.[5] and others. A short review of the definitions and the physical meaning of the invariants of the velocity gradient tensor $\mathsf{G} = \nabla \boldsymbol{u}$ are given here for incompressible flow. Namely:

$$P_{\mathsf{G}} = -tr(\mathsf{G}) = -\nabla \cdot \boldsymbol{u} = 0, \tag{9}$$

$$Q_{\mathsf{G}} = -\frac{1}{2}tr(\mathsf{G}^2) = \frac{1}{4}\left[\boldsymbol{\omega}^2 - 2tr(\mathsf{S}^2)\right] = Q_{\Omega} + Q_{\mathsf{S}}, \tag{10}$$

$$R_{\mathsf{G}} = -det(\mathsf{G}) = -\frac{1}{3}tr(\mathsf{G}^3) = -\frac{1}{3}\left[tr(\mathsf{S}^3) + 3tr(\Omega^2\mathsf{S})\right] = R_{\mathsf{S}} - tr(\Omega^2\mathsf{S}), \tag{11}$$

where P_{G}, Q_{G} and R_{G} are the first, second and third invariant of G, respectively. It is useful to recall that G can be decomposed into its symmetric and antisymmetric parts, $\mathsf{S} = 1/2(\mathsf{G}+\mathsf{G}^t)$ and $\Omega = 1/2(\mathsf{G} - \mathsf{G}^t)$, respectively, where S denotes the rate-of-strain tensor, and Ω is the rate-of-rotation tensor. Their invariants play an important role in the identification of coherent structures[3,5,7,9], and the development of new turbulence models[37]. For example, the second invariant $Q_{\Omega} = -1/2tr(\Omega^2) = 1/4|\boldsymbol{\omega}|^2$ is proportional to the enstrophy density. Therefore, it identifies tube-like structures with high vorticity $\boldsymbol{\omega} = \nabla \times \boldsymbol{u}$. The invariant $Q_{\mathsf{S}} = -1/2tr(\mathsf{S}^2) = -1/4(\epsilon/\nu)$ is proportional to the local rate of viscous dissipation, $\epsilon = 2\nu\mathsf{S} : \mathsf{S}$. Notice that $Q_{\Omega} \geq 0$ and $Q_{\mathsf{S}} \leq 0$ and these two invariants are related to Q_{G} with the identity (10). Hence, positive values of $Q_{\mathsf{G}} > 0$ are related to areas of enstrophy domination over viscous dissipative straining. Another important term is the third invariant of S i.e. $R_{\mathsf{S}} = -1/3tr(\mathsf{S}^3)$. It constitutes a part of the straining production (see Eq. 17), and R_{G} in the identity (11). Moreover, it correlates the three eigenvalues of S as $R_{\mathsf{S}} = -\sigma_1\sigma_2\sigma_3$, where $\sigma_1 \geq \sigma_2 \geq \sigma_3$ are arranged in a descending order. Due to incompressibility, the sum $\sigma_1 + \sigma_2 + \sigma_3 = 0$, and the sign of R_{S} follows the sign of the intermediate eigenvalue to categorise the structures shape to tube-like $R_{\mathsf{S}} < 0$ or sheet-like $R_{\mathsf{S}} > 0$. Generally speaking, when $R_{\mathsf{G}} < 0$ and $Q_{\mathsf{G}} \gg 0$, a positive enstrophy production is prevalent, and stable tube-like vortex stretching structures (the so-called worms) predominate the vorticity
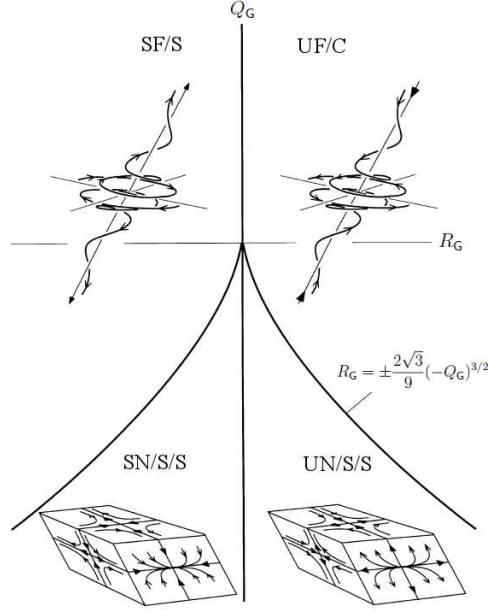
FIG. 4: Classification of local flow topology following $(Q_\mathsf{G}, R_\mathsf{G})$ invariants of velocity gradient tensor for incompressible flow [taken from Ooi *et al.*[5], reproduced with permission from A. Ooi, J. Martin, J. Soria and M. S. Chong, J. Fluid Mech **381**, 141–174 (1999). Copyright 1999, Cambridge University Press] with SF/S: stable focus/stretching, SN/S/S: stable node/saddle/saddle, UN/S/S: unstable node/saddle/saddle and UF/C: unstable focus/compressing.

compression. However, when $R_\mathsf{G} > 0$ and $Q_\mathsf{G} \ll 0$, the straining production becomes the dominant one and associates mostly with strong and unstable sheet-like viscous dissipative structures. Figure 4 shows the four main classes of the possible flow topology in $(Q_\mathsf{G}, R_\mathsf{G})$ phase plane taken from Ooi *et al.*[5], where more details thereof can be found in the above references.

A.   Universal aspects of turbulence structures

Many turbulent flows have revealed an inclined "teardrop" shape of the joint PDF $(Q_\mathsf{G}, R_\mathsf{G})$, which has been speculated as a kind of universality in the space of invariants[2]. Despite the different global flow geometries created in many types of turbulence, *e.g.* an isotropic turbulence[5], turbulent boundary layer[6], turbulent channel flow[7] and others[8,9], all displayed the same feature of preferred $(Q_\mathsf{G}, R_\mathsf{G})$ statistical correlation in areas dominated

14

by small-scale vortex stretching and viscous dissipation structures. This behaviour as a common aspect of 3D turbulence and its Gaussian-deviation property, is extended here to include the buoyancy-driven flows in a Rayleigh-Bénard framework at hard turbulent regime.
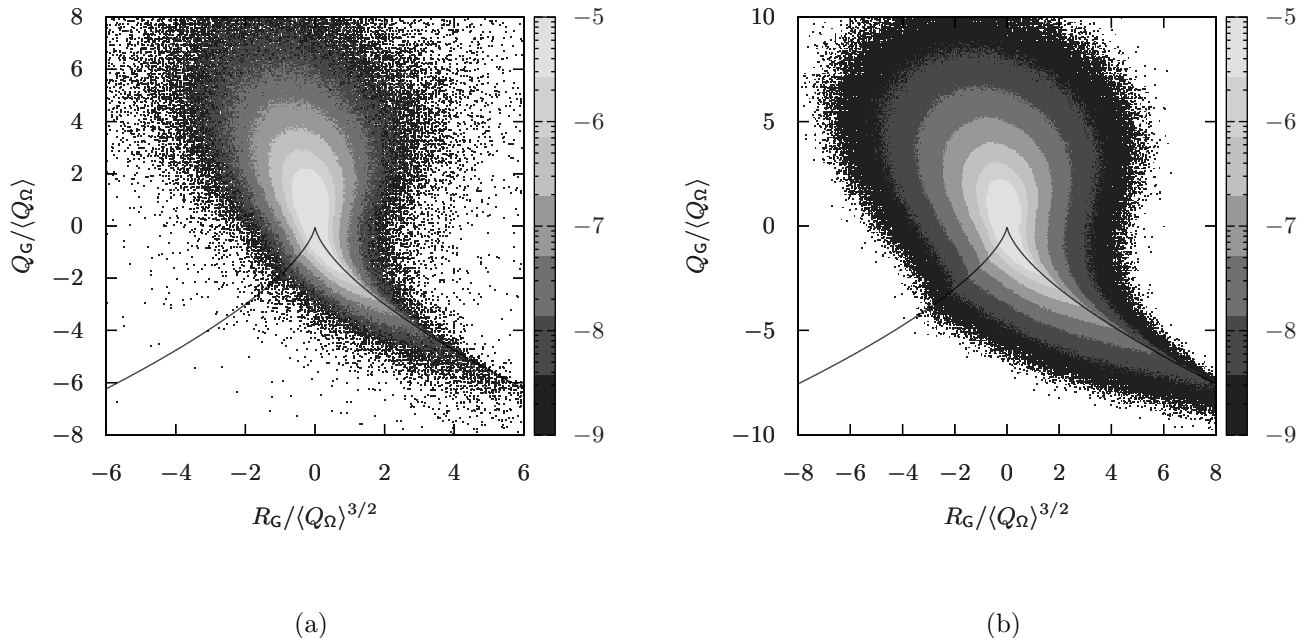

(a)   (b)

FIG. 5: Joint PDF of normalized Q_G and R_G invariants on logarithmic scale at (a) $Ra = 10^8$ and (b) $Ra = 10^{10}$ through the bulk (V_{bulk}), where the solid black line represents the null-discriminant curve $D_\mathsf{G} = (27/4)R_\mathsf{G}^2 + Q_\mathsf{G}^3 = 0$.

To do so, the joint PDFs of Q_G and R_G invariants through the bulk (V_{bulk}), have been plotted in Figure 5. The invariants are normalized using $\langle Q_\Omega \rangle$ (following Ooi et $al.$[5]) to show the same "teardrop" shape as a universal feature of the small scale motions in both turbulent cases. As can be seen, Figures 5a and 5b indicate that most of the flow domain is occupied by coherent dynamics of small mean gradients around the origin; while the rest of the flow $i.e.$ fluctuations and small scales, obey substantially stable tube-like focus/stretching structures ($Q_\mathsf{G} > 0$ and $R_\mathsf{G} < 0$), and unstable sheet-like node/saddle/saddle topologies ($Q_\mathsf{G} < 0$ and $R_\mathsf{G} > 0$ the so-called Vieillefosse tail).
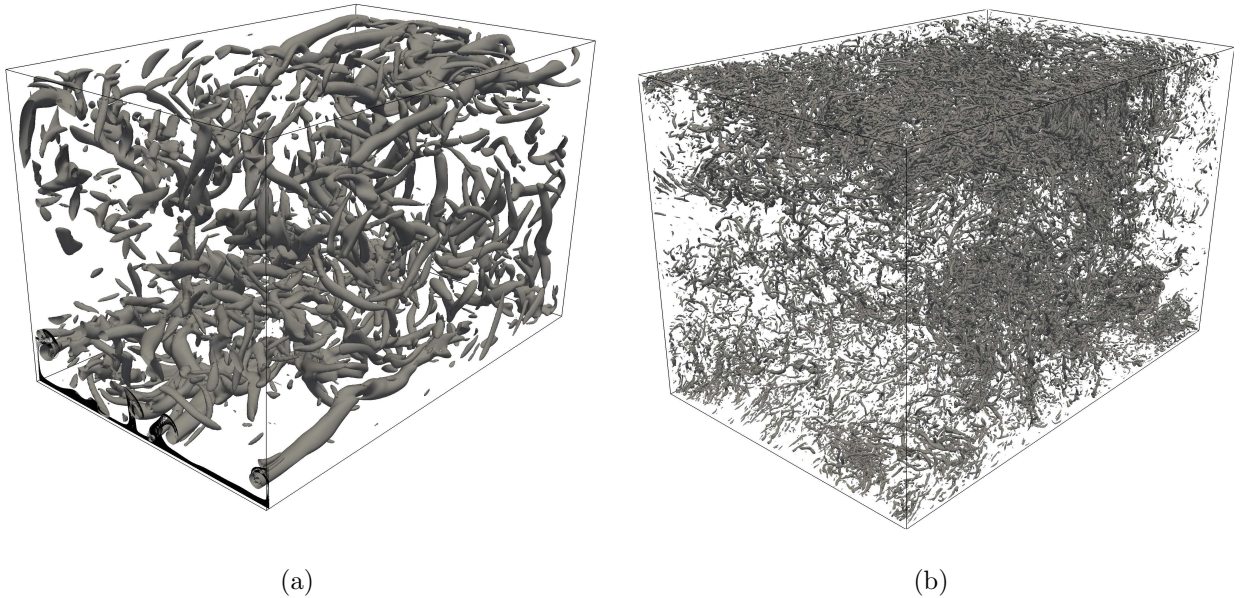
15

FIG. 6: Structures of Q_{G} positive values drawn in a portion of the domain for (a) $Ra = 10^8$ ($Q_{\mathsf{G}} > 14.29$) and (b) $Ra = 10^{10}$ ($Q_{\mathsf{G}} > 128.9$). (See movies of their dynamics MULTIMEDIA VIEW). The solid black contours in (a) indicate the hot thermal plumes.

In order to gain an understanding of the spatial structure of turbulence, an instantaneous 3D visualization of Q_{G} iso-surface at high positive values is plotted in Figure 6. The structures take the shape of the so-called worms[2], which are classified as stable tube-like focal stretching topology of intensive enstrophy values. As can be seen in Figure 6a, the worms are characterized by large fragmentations with an elliptical cross-section in the case of $Ra = 10^8$. They seem to be aligned in many places with the evolution of the thermal plumes (hot 2D black contours), which expand in the bulk to support the prevalence of the tube-like rotational topology.

Plotting the joint PDF map of Q_Ω and $-Q_{\mathsf{S}}$ invariants can provide significant physical information about the dominant flow topologies respect to the kinetic energy dissipation. For example, points of high enstrophy (Q_Ω), but very small dissipation ($-Q_{\mathsf{S}}$), indicate solid-body rotational structures (vortex tubes), while points of strong dissipation but little enstrophy represent irrotational straining domination. Balanced distribution of $Q_\Omega = -Q_{\mathsf{S}}$ translates a vortex sheet topology that normally occurs in the BLs. As shown in Figures 7a and 7b, the flow topology is mainly tube-like rotational in the bulk region, where the highest local value of $-Q_{\mathsf{S}}$ is smaller than the highest local value of Q_Ω, and the joint PDF is skewed
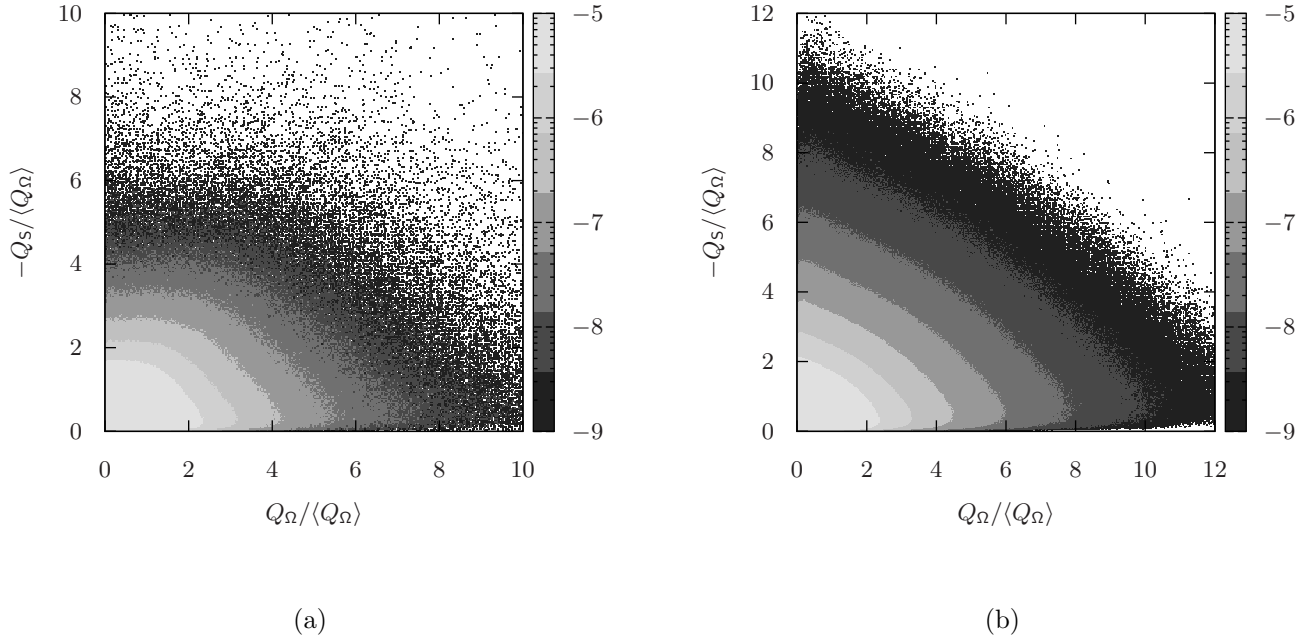
FIG. 7: Joint PDF of normalized Q_Ω and $-Q_\mathsf{S}$ invariants on logarithmic scale at (a) $Ra = 10^8$ and (b) $Ra = 10^{10}$, through the bulk (V_{bulk}).

towards high Q_Ω with long-lived solid-body rotation.

When the flow becomes significantly turbulent at $Ra = 10^{10}$, the turbulent background velocity derivatives as $-Q_\mathsf{S}$ (the viscous strain and Q_Ω in concomitant), get self-amplified[2]. They often surpass the original large-scale forces generated here by buoyancy, as reported by Tsinober[2]. This self-growing of turbulent dissipation $-Q_\mathsf{S}$ can be clearly identified in the $(Q_\Omega, -Q_\mathsf{S})$ map in Figure 7b. It works on contracting the worms to be composed in smaller and numerous fragments within the bulk (see Figure 6b). Physically, the nonlinearities as the enstrophy production $(4tr(\Omega^2\mathsf{S}) = \boldsymbol{\omega} \cdot \boldsymbol{\omega}\mathsf{S})$, become increased, and conduct the local growing of the strain-dominated regions. While, an enhanced equilibrium between these nonlinearities (e.g. the vortex-stretching vector $\boldsymbol{\omega}\mathsf{S}$), and its viscous destruction $(Pr/Ra)^{1/2}\boldsymbol{\omega}\nabla^2\boldsymbol{\omega}$ take place mostly in regions of enstrophy concentrations (i.e. the worms)[2]. These processes are explained and justified in detail by Tsinober[2]. They are essentially interconnected in

17

the frame of the enstrophy transport equation:

$$\frac{1}{2}\frac{D|\boldsymbol{\omega}|^2}{Dt} = \boldsymbol{\omega}\cdot\boldsymbol{\omega}\mathsf{S} + \sqrt{\frac{Pr}{Ra}}\boldsymbol{\omega}\nabla^2\boldsymbol{\omega} + \boldsymbol{\omega}\cdot\nabla\times\boldsymbol{f}, \tag{12}$$

and the transport equation of the strain product $\mathsf{S}^2/2$ (Eq. 17). Following Tsinober[2], these events are normally associated with (i) large strain (as outlined above), (ii) high alignment of vorticity with the most extensional eigenstrain $\boldsymbol{\lambda}_1$ (observed below), and (iii) strong tilting of worms (visible in Figure 6b).

Similarly to many turbulent flows we notice the preferential alignment between $\boldsymbol{\omega}$ and $\boldsymbol{\lambda}_2$, the intermediate eigenvector of the rate-of-strain tensor S, in both turbulent cases. PDF charts of $\cos(\boldsymbol{\omega},\boldsymbol{\lambda}_i) = (\boldsymbol{\omega}\cdot\boldsymbol{\lambda}_i)/(|\boldsymbol{\omega}||\boldsymbol{\lambda}_i|)$ have been plotted within the bulk in Figure 8a to manifest the general common feature of the geometrical structure in 3D turbulence. This alignment becomes of notable importance in turbulent dynamics since it contributes to the enstrophy generation term given by $\boldsymbol{\omega}\cdot\boldsymbol{\omega}\mathsf{S} = \boldsymbol{\omega}^2\sigma_i\cos^2(\boldsymbol{\omega},\boldsymbol{\lambda}_i)$. One of the noteworthy remarks is the high probability observed at $\cos(\boldsymbol{\omega},\boldsymbol{\lambda}_1) = \pm1$ for $Ra = 10^{10}$ in comparison with $Ra = 10^8$. It indicates a slightly enhanced alignment between $\boldsymbol{\omega}$ and $\boldsymbol{\lambda}_1$ to follow the self-amplified $-Q_\mathsf{S}$ regions and, therefore, assists the linear contributions of vortex-stretching term. In other words, these self and local strain growing regions at $Ra = 10^{10}$, contribute to local effects associated with (self) interactions of $\boldsymbol{\omega}$ and S^2. However, we cannot generalize these events (with Ra increment), as many issues, $i.e.$ the increased nonlinear enstrophy production, predominant nonlocality and interactions between large and small scales, are essential in vortex-stretching origins. For example, within a frame of forced, homogeneous, isotropic turbulence, Hamlington $et\ al.$[38] have reported a preferential alignment of vorticity with the most extensional eigenvector of the $nonlocal$ (background) strain. Namely, they decompose the strain rate into its $local$ part $i.e.$ the self-induced strain field within the vicinity of a typical vortical structure, and its $nonlocal$ part, where the strain is essentially induced by all the surrounding other vorticities outside the vortical structure. They found that the vorticity is preferentially aligned with the most extensional background strain rate eigenvector to support the linear contribution to the vortex-stretching dynamics. Hence, this may lead us to the assumption that when the flow is extremely turbulent, the characteristic flow scales get smaller, and the vorticities lay closer and become correlated. As a result, the background-strain $(\boldsymbol{\omega},\boldsymbol{\lambda}_1)$ alignment arises and combines with the local-based one to

eventually yield a general enhancement of *local* interaction $\boldsymbol{\omega}/\mathsf{S}$.

Another important alignment defined by $\cos(\boldsymbol{\omega}, \boldsymbol{\omega}\mathsf{S}) = \sigma_i \cos^2(\boldsymbol{\omega}, \boldsymbol{\lambda}_i) / \{\sigma_i^2 \cos^2(\boldsymbol{\omega}, \boldsymbol{\lambda}_i)\}^{1/2}$ is outlined in this study, as a universal feature. Again, it emphasizes on the predominant vortex-stretching action through the bulk, and the net enstrophy production is always positive *i.e.* $\langle \boldsymbol{\omega} \cdot \boldsymbol{\omega}\mathsf{S} \rangle > 0$, in the two turbulent cases. As shown in Figure 8b, both distributions are identically asymmetric and positively-skewed, which probably corresponds to the events associated with strong alignment between vorticity and the intermediate eigenstrain vector $\boldsymbol{\lambda}_2$.
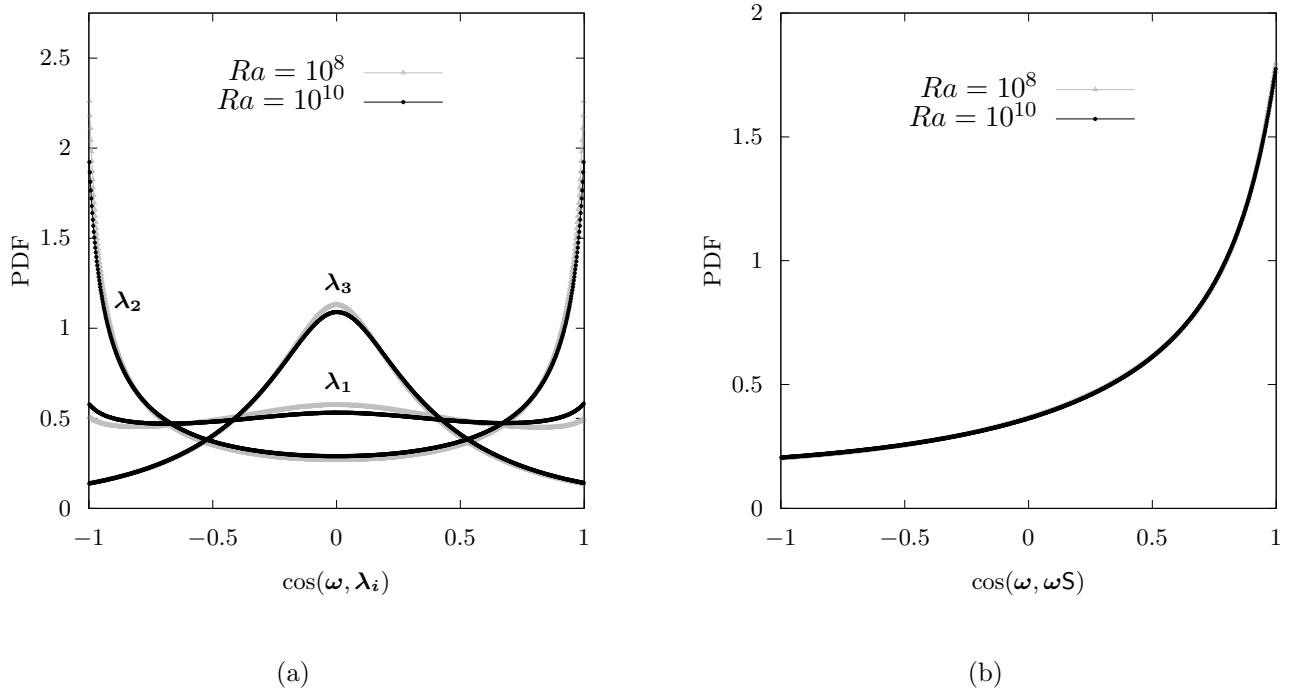

(a)

(b)

FIG. 8: PDF of vorticity alignments with the eigenvectors of the rate-of-strain tensor (a) and the vortex-stretching vector $\boldsymbol{\omega}\mathsf{S}$ (b), through the bulk region (V_{bulk}).

B. Dynamics of Q_G and R_G invariants

The joint PDFs of $(Q_\mathsf{G}, R_\mathsf{G})$ invariants have provided a statistical picture of the most prevalent distribution for the flow topology and structures, averaged in time and volume. Nonetheless, studying the evolution of Q_G and R_G invariants in a Lagrangian frame allows a dynamical observation of the 3D small-scale turbulence mechanisms, such as the vortex stretching and turbulent kinetic dissipation. Namely, in the frame of a moving observer following a fluid particle, the local surrounding flow structures are essentially described by G and its Galilean invariants, *i.e.* Q_G and R_G. They change in time throughout their lifetime to be finally destroyed in average and leave the large scales of the coherent uniform flow. This change can be interpreted by the Lagrangian dynamics of invariant quantities that were first studied by Cantwell[39]. He deduced the evolution equations for Q_G and R_G and found an analytical solution, but for the inviscid Euler equations. A procedure to investigate the average dynamical behaviour of the invariants was proposed by Martín *et al.*[4] and Ooi *et al.*[5] who used a conditional averaging technique of the invariant rates in DNS of isotropic turbulence. Recalling the deduction by Cantwell[39], firstly, the evolution equation of G can be obtained by taking the gradient of NS equations, yielding:

$$\frac{D\mathsf{G}}{Dt} + \mathsf{G}^2 = -\mathsf{H}(p) + \sqrt{\frac{Pr}{Ra}}\nabla^2\mathsf{G} + \nabla\boldsymbol{f}, \tag{13}$$

where $\mathsf{H}(\phi) = \nabla\nabla\phi$ is the Hessian of a scalar field ϕ. Then, using the definitions of the invariants (Eqs.10 and 11), the evolution equations of Q_G and R_G read as:

$$\frac{DQ_\mathsf{G}}{Dt} = -3R_\mathsf{G} - tr(\mathsf{G}\mathsf{H}_\mathsf{G}), \qquad \frac{DR_\mathsf{G}}{Dt} = \frac{2}{3}Q_\mathsf{G}^2 - tr(\mathsf{G}^2\mathsf{H}_\mathsf{G}), \tag{14}$$

where H_G is a second-order tensor which includes the resultant pressure Hessian, diffusive and the buoyancy terms as:

$$\mathsf{H}_\mathsf{G} = -\left(\mathsf{H}(p) - \frac{2Q_\mathsf{G}}{3}\mathsf{I}\right) + \sqrt{\frac{Pr}{Ra}}\nabla^2\mathsf{G} + \nabla\boldsymbol{f}, \tag{15}$$

where I is the identity matrix.

The left-hand sides in Eqs.(14), *i.e.* DQ_G/Dt and DR_G/Dt, are analysed using an averaging approach identical to Ooi *et al.*[5] and Elsinga and Marusic[6]. Namely, the mean temporal rate of change in the invariants Q_G and R_G is computed from a set of instantaneous flow

20

fields conditionally upon the invariants themselves. The corresponding approach reads as:

$$\left\langle \frac{DQ_\mathsf{G}}{Dt}|(Q_\mathsf{G}^0, R_\mathsf{G}^0)\right\rangle = \left\langle \frac{DQ_\mathsf{G}}{Dt}| -\frac{1}{2} \leq \frac{(Q_\mathsf{G} - Q_\mathsf{G}^0)}{\Delta Q_\mathsf{G}} < \frac{1}{2}; -\frac{1}{2} \leq \frac{(R_\mathsf{G} - R_\mathsf{G}^0)}{\Delta R_\mathsf{G}} < \frac{1}{2}\right\rangle,$$
$$\left\langle \frac{DR_\mathsf{G}}{Dt}|(Q_\mathsf{G}^0, R_\mathsf{G}^0)\right\rangle = \left\langle \frac{DR_\mathsf{G}}{Dt}| -\frac{1}{2} \leq \frac{(Q_\mathsf{G} - Q_\mathsf{G}^0)}{\Delta Q_\mathsf{G}} < \frac{1}{2}; -\frac{1}{2} \leq \frac{(R_\mathsf{G} - R_\mathsf{G}^0)}{\Delta R_\mathsf{G}} < \frac{1}{2}\right\rangle,$$

(16)

where $(Q_\mathsf{G}^0, R_\mathsf{G}^0)$ are the center coordinates of the bin size $(\Delta Q_\mathsf{G}, \Delta R_\mathsf{G})$ over which the material derivative is averaged. An imposed bin size 0.05×0.1 in the range $-1 \leq R_\mathsf{G}/\langle Q_\Omega\rangle^{3/2} \leq 1$ and $-2 \leq Q_\mathsf{G}/\langle Q_\Omega\rangle \leq 2$, respectively in the area of interest, is used. It fulfills a good converging of rates with a robust number of samples (> 500 per bin). The averaged rates are expressed as vectors of two components $(\langle DQ_\mathsf{G}/Dt\rangle, \langle DR_\mathsf{G}/Dt\rangle)$ and plotted together with their integrated mean trajectories in Figure 9 for both Ra-number cases through the bulk.

Similarly to isotropic turbulence[4,5], the trajectories are cyclically decaying towards the origins, moving on average, from regions of higher velocity gradients (small scale motions/fluctuations) to regions of smaller ones (large coherent scales) near the origin. They intrinsically indicate a clockwise spiraling change of the local flow topology around a fluid particle from unstable node saddle/saddle (UN/S/S), stable node saddle/saddle (SN/S/S), stable focus/stretching (SF/S) to unstable focus/compressing (UF/C). A scenario for the mean evolution of fluid particles was given by Ooi *et al.*[5] from that behaviour of the conditional mean trajectories. Namely, within the neighbourhood of coherent focal structure (SF/S), a fluid particle that stands there, in location probably UN/S/S topology ($R_\mathsf{G} > 0, D_\mathsf{G} < 0$), will be sucked rapidly into the core of that elongated (intensive enstrophy) structure where the pressure is essentially low. The local topology around the particle changes from UN/S/S via SN/S/S to SF/S. Due to the vortex expansion, the particle travels along the core to regions where those focal structures lose their compact nature (at the ends and bends) by contraction, and the topology becomes UF/C. The compressing actions change the sign of DQ_G/Dt, and reduce the magnitude of invariants to support the decaying events. These events are rendered as an interplay of the non-local pressure Hessian with the viscous diffusion and energy-injecting terms (recent insights about these effects are available for the reader in Wilczek[40], and mainly in the references therein). It attenuates the evolution speed (proportional to the vector length) across the null-discriminant $D_\mathsf{G} = (27/4)R_\mathsf{G}^2 + Q_\mathsf{G}^3 = 0$ curve at $R_\mathsf{G} > 0$, and appears in opposite sign with damping effect to DQ_G/Dt and DR_G/Dt in Eqs.(14). The developed topology becomes nodal (UN/S/S)

21
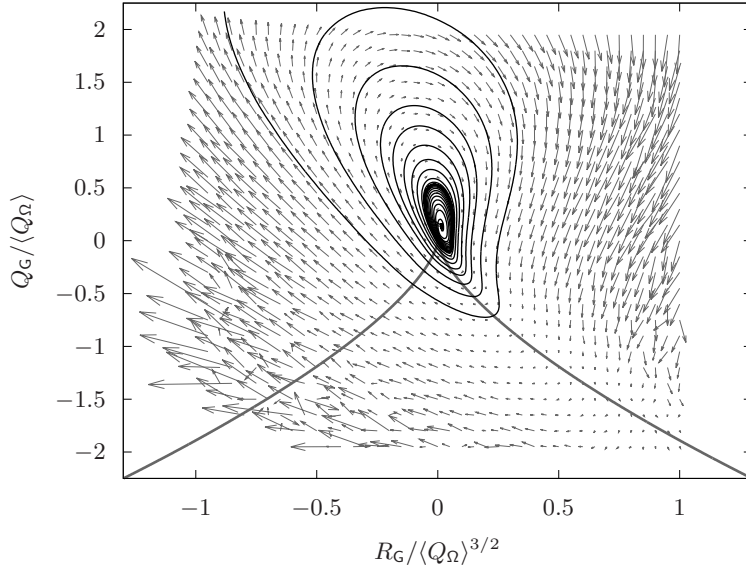
(a)
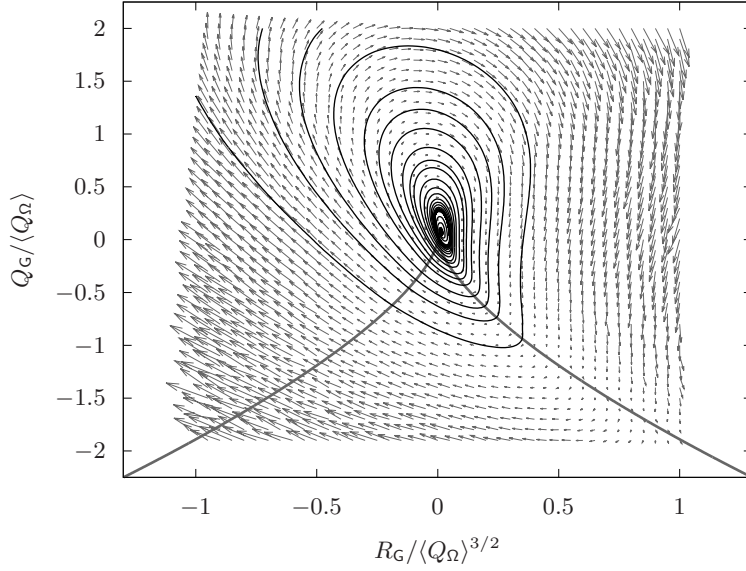
(b)

FIG. 9: Conditional mean vectors of $\langle DQ_{\mathsf{G}}/Dt \rangle$ and $\langle DR_{\mathsf{G}}/Dt \rangle$ in $(Q_{\mathsf{G}}, R_{\mathsf{G}})$ plane together with their integral trajectories (black solid orbits) at (a) $Ra = 10^8$ and (b) $Ra = 10^{10}$, through the bulk (V_{bulk}), where the bold solid line indicates $D_{\mathsf{G}} = 0$.

and under the dissipative actions, the trajectories are twisted upwards converging to the origin instead of continuing towards higher values of $R_{\mathsf{G}} > 0$ asymptotic to $D_{\mathsf{G}} = 0$ curve in

the case of inviscid Eulerian model ($\mathsf{H_G} = 0$)[39]. Comparing the two scenarios in Figure 9, one can note the influence of the local self-amplified velocity gradient (growing $-Q_\mathsf{S}$), which is probably induced by the nonlinear advection[39,40]. It contracts the structures further, and bend the trajectories inwards in the area of $D_\mathsf{G} > 0$ and $R_\mathsf{G} > 0$, at $Ra = 10^{10}$ (Figure 9b).

Analogously to the previous studies[4–6], the averaged trajectories have revealed that possible periodic spiralling before converging to the origin. The period measurements identified here regarded to one periodic orbit T_0, read $6.7[TU]$ and $4.8[TU]$, correspondingly for $Ra = 10^8$ and 10^{10}, which are suspected to be proportional to the characteristic lifetimes of energy containing eddies released in the bulk. They are found to be close to the periods of the estimated large eddy turnover time $T_0 \sim \tau_{eddy}$ indicating a shorter lifetime of the large coherent eddies in the bulk at the higher Ra-number case. This is not surprising since the large-scale eddies break up under the events associated with the self-amplification of G ($-Q_\mathsf{S}$ and Q_Ω) at $Ra = 10^{10}$. Broadly speaking, the turbulence type in the core region of RBC is found to be comparable, in statistical aspects, with the isotropic nature. For example, the joint PDF map of ($Q_\Omega, -Q_\mathsf{S}$) invariants displayed in Figure 7a presents a similar distribution as the forced isotropic turbulence investigated in Ooi et $al.$[5]. However, the present proportionality T_0 in respect to τ_{eddy}, differs from that outlined by Ooi et $al.$[5], who reported a factor of three times $T_0 \sim 3\tau_{eddy}$. This discrepancy could be returned to the confined configuration of our RBC (adiabatic sidewalls) as well as the mechanism of the thermal plumes in injecting the kinetic energy to the large-scale eddies. Indeed, the measured periods T_0 can be compared to the average plume lifetime τ_{pl} with almost three times factor $T_0 \sim 3\tau_{pl}$. Here, $\tau_{pl} \sim \delta_T^2 \sqrt{RaPr}$ is defined as the plume lifetime through which it detaches with the thickness of the thermal BL δ_T, and loses its temperature contrast by the thermal diffusivity $1/\sqrt{RaPr}$[13]. Following this approach, the determined average plume lifetimes in the current configurations read $\tau_{pl} \sim 2.190[TU]$ and $1.276[TU]$ for $Ra = 10^8$ and 10^{10}, respectively. These findings accordingly suggest the participation of the thermal plumes in the large-scale kinetic energy containing eddies and turbulent wind, especially when the plumes (mushroom-like) elongate importantly in the bulk before scattering. However, in a hard turbulent state at high Ra number such as 10^{10}, the role of plumes is outstandingly reduced due to the extreme fluctuations and the good mixing. Consequently, the role of the self-amplified $-Q_\mathsf{S}$ in creating the large-scale eddies in the bulk is enlarged. This could be the reason why

the measured period T_0 exceeds somewhat the $3\tau_{pl}$, which confirms the prevalence of the self-amplified velocity derivatives by turbulence over the buoyant mechanisms.

C.   Dynamics of R_{S} and $tr(\Omega^2\mathsf{S})$ nonlinearities

In order to elucidate the impact of the local self-amplification of G (at least at high Ra numbers) more, the dynamics of the physically meaningful third-moment nonlinearities described by the enstrophy production $R_{\mathsf{S}} - R_{\mathsf{G}} = tr(\Omega^2\mathsf{S})$, and the quantity R_{S} (as a contribution of the straining production) have been studied. They both constitute the production term of the strain product $\mathsf{S}^2/2 \sim -Q_{\mathsf{S}}$ inside the transport equation, which reads as:

$$\frac{DQ_{\mathsf{S}}}{Dt} = -3R_{\mathsf{S}} + tr(\Omega^2\mathsf{S}) - tr(\mathsf{SH_S}), \tag{17}$$

with

$$\mathsf{H_S} = -\left(\mathsf{H}(p) - \frac{2Q_{\mathsf{G}}}{3}\mathsf{I}\right) + \sqrt{\frac{Pr}{Ra}}\nabla^2\mathsf{S} + 1/2(\nabla\boldsymbol{f} + \nabla\boldsymbol{f}^t). \tag{18}$$

In the frame of an isotropic turbulence, statistical analysis of these nonlinearities, as the joint PDF $(R_{\mathsf{S}} - R_{\mathsf{G}}, R_{\mathsf{S}})$, was earlier performed by Kholmyansky *et al.*[41]. It revealed that the two such nonlinearities, namely, enstrophy and strain productions, are locally different and only weakly correlated. Others like Lüthi *et al.*[42], again for isotropic turbulence, have stressed on the importance of these nonlinearities by studying the evolution of the small scale motions in a 3D phase space $\{Q_{\mathsf{G}}, R_{\mathsf{S}}, R_{\mathsf{S}} - R_{\mathsf{G}}\}$.

In this work and in the bounds of V_{bulk}, the joint PDFs of $(R_{\mathsf{S}} - R_{\mathsf{G}}, R_{\mathsf{S}})$ are plotted in Figure 10 for both turbulent cases. The two invariant-based terms are normalized by $\langle Q_\Omega\rangle^{3/2}$, differently than in[41] where therein, the mean values $\langle R_{\mathsf{S}} - R_{\mathsf{G}}\rangle$ and $\langle R_{\mathsf{S}}\rangle$ are respectively used for $R_{\mathsf{S}} - R_{\mathsf{G}}$ and R_{S}. In consistency with Kholmyansky *et al.*[41], the two plots have shown a similar weak correlation locally of the two nonlinearities, but with different behaviour in the positive part of both. They reveal the presence of many points with large positive values of both nonlinearities, slightly shifted toward $R_{\mathsf{S}} > 0$. Comparing the two charts in Figures 10a and 10b, one can note the enhanced tendency of the distribution at $Ra = 10^{10}$ to be more linear with balanced nonlinearities in regions of vortex stretching and positive strain production. This can imply an enhanced localization to the nonlinearities in the regions dominated by the self-amplified strain, which corresponds to the observations
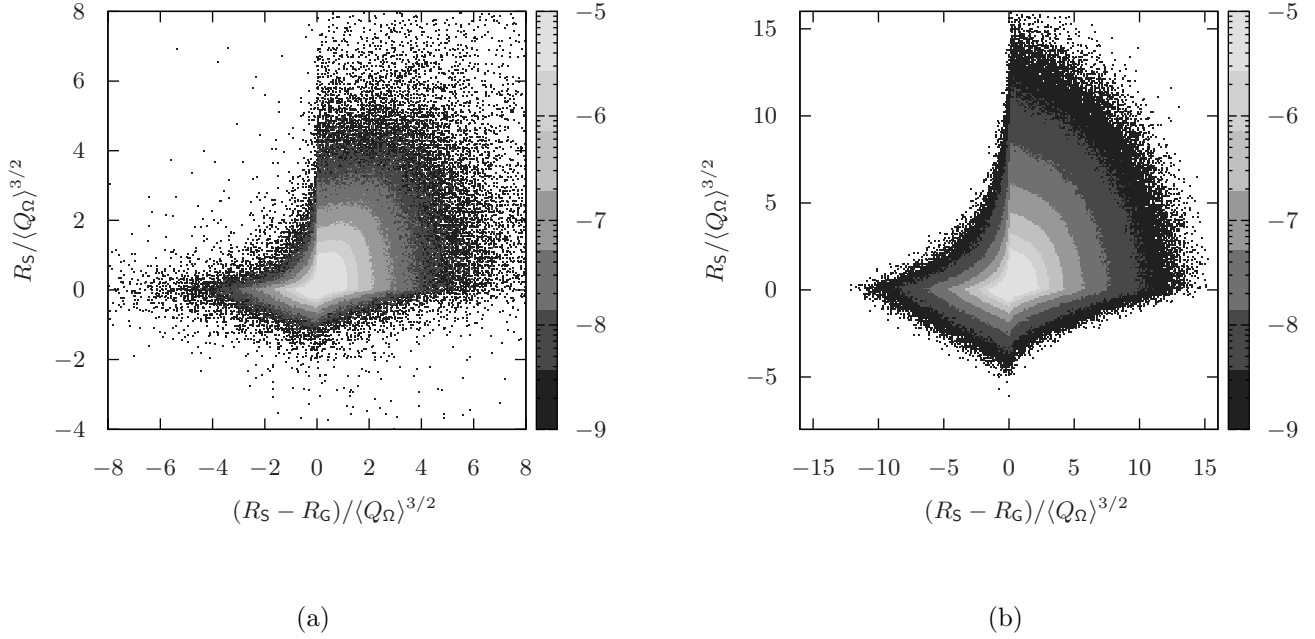
FIG. 10: Joint PDF of normalized $R_S - R_G$ and R_S invariants on logarithmic scale at (a) $Ra = 10^8$ and (b) $Ra = 10^{10}$ through the bulk (V_{bulk}).

outlined in Section III A. Namely, at $Ra = 10^{10}$, a local self-amplification of G ($-Q_S$ and Q_Ω in concomitant) takes place and produces simultaneously an increase in the nonlinearity of vortex stretching (in slots of S^2) with enhanced local interactions of vorticity/strain.

Following an identical procedure to $(DQ_G/Dt, DR_G/Dt)$ in the previous Section, the conditional mean trajectories of $(D(R_S - R_G)/Dt, DR_S/Dt)$ have been plotted in Figure 11 for both turbulent cases in the bulk. As can be seen, the two mean dynamics show a zero starting point since with no straining, no enstrophy will evolve and vice versa[2]. The trajectories start moving towards negative values of enstrophy production to emphasize always on the collaborated role between the vortex compression structures and the strain generation. When $R_S > 0$ the vectors suddenly change their signs to travel upwards with a notably enhanced linear evolution at $Ra = 10^{10}$ (see Figure 11b). The directional change can be returned to the opposite sign of these quantities in the production term of the strain rate $-Q_S$, inside Eq.(17). In agreement with the previous notes, the self-amplified viscous
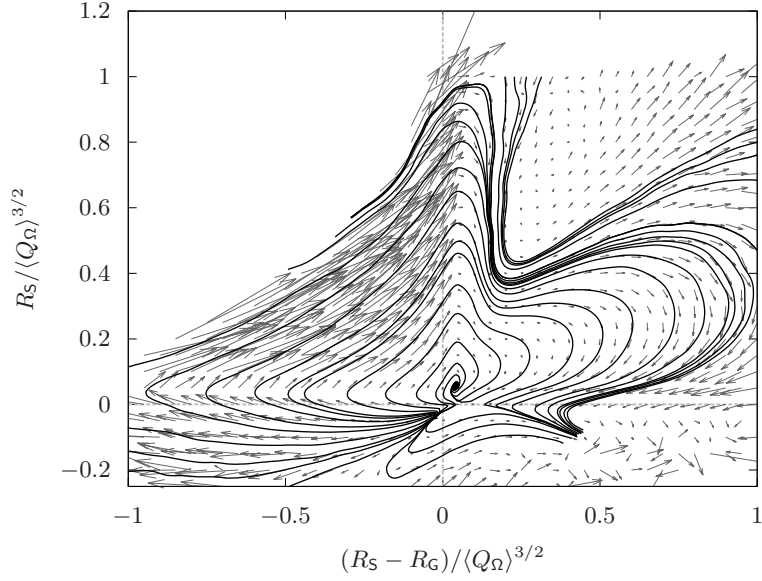
(a)
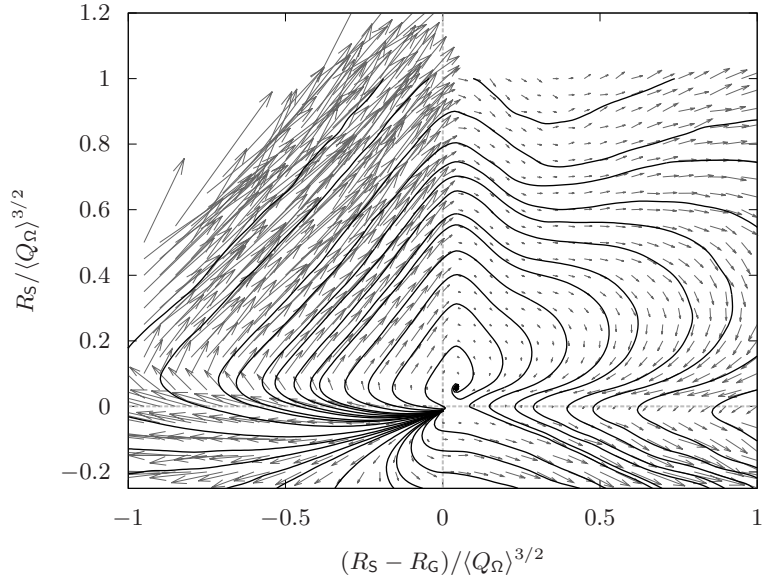
(b)

FIG. 11: Conditional mean vectors of $\langle DR_{\mathsf{S}}/Dt \rangle$ and $\langle D(R_{\mathsf{S}} - R_{\mathsf{G}})/Dt \rangle$ in $(R_{\mathsf{S}}, R_{\mathsf{S}} - R_{\mathsf{G}})$ plane together with their integral trajectories (black solid lines) at (a) $Ra = 10^8$ and (b) $Ra = 10^{10}$, in the bulk (V_{bulk}).

strain $-Q_{\mathsf{S}}$ at the higher Ra number is apparently recognized through further contraction of vorticities ($R_{\mathsf{S}} - R_{\mathsf{G}} < 0$) and growing strain regions ($R_{\mathsf{S}} > 0$), which is revealed in higher

26

linear and organized act of trajectories in that zones. This confirms again the direct and local assistance of vortex compression to the dissipative actions and energy cascade[2] (in a hard turbulence case). Afterwards, once the evolution enters the stretching area ($R_\mathsf{S} - R_\mathsf{G} > 0$), a sharp decay towards the small values of R_S takes place at $Ra = 10^8$ (Figure 11a). This displacement could be returned to the nonlocality effect since we are in the centered vorticity tube-like filaments/worms. However, at the higher Ra number the trajectories tend to move more softly indicating the improved localization of nonlinearities in those areas. It is sustained by strong linear interactions in regions of ($R_\mathsf{S} > 0$ and $R_\mathsf{S} - R_\mathsf{G} < 0$), which in turn make a positive contribution to the magnitude of the vortex-stretching vector $\boldsymbol{\omega}\mathsf{S}^2$. Finally, the mean trajectories spiral inwards converging in part towards the origin. They tend to either return to the starting point close to the origin, or change their direction to higher values across $R_\mathsf{S} < 0$ and $R_\mathsf{S} - R_\mathsf{G} > 0$, again, with higher linearity at $Ra = 10^{10}$. It is important to note the positive end (origin) of ($\langle D(R_\mathsf{S} - R_\mathsf{G})/Dt\rangle, \langle DR_\mathsf{S}/Dt\rangle$), which asserts the predominance of vortex stretching ($\langle \boldsymbol{\omega} \cdot \boldsymbol{\omega}\mathsf{S}\rangle > 0$), and the concomitant predominant self-amplification of viscous strain/dissipation production ($R_\mathsf{S} > 0$), generally happening in 3D turbulence[2].

IV. INVARIANTS OF THE VELOCITY-TIMES-TEMPERATURE GRADIENT TENSOR

Hereafter we consider the gradient of velocity multiplied by temperature tensor $\mathsf{G}_\theta = \nabla(\boldsymbol{u}T)$, which couples the kinetic and thermal small scales of motions. Notice that $\boldsymbol{u}$ and T are defined in such a way that $\int_\Omega \boldsymbol{u}d\Omega = 0$ and $\int_\Omega \langle T\rangle d\Omega = 0$. This tensor contributes to the turbulent heat flux and buoyant production, given as $\langle w'T'\rangle$, which is found to be directly associated with the evolution of thermal plumes[14]. On the other hand, its invariants (such as the magnitude $|\mathsf{G}_\theta| = (\mathsf{G}_\theta : \mathsf{G}_\theta)^{1/2}$) address in some sense, strong interactions of kinetic and thermal dissipation rates. Namely, $\mathsf{G}_\theta = T\mathsf{G} + \boldsymbol{u} \otimes \nabla T$, when T is constant, yields to $\mathsf{G}_\theta \sim \mathsf{G}$ and hence, $|\mathsf{G}_\theta|^2 \sim |\mathsf{G}|^2 = |\Omega|^2 + |\mathsf{S}|^2$. The strain part therein, is proportional to the local viscous dissipation ϵ, as $|\mathsf{S}|^2 = \mathsf{S} : \mathsf{S} = tr(\mathsf{S}^2) = 1/2(Pr/Ra)^{-1/2}\epsilon$. On the other hand, when $|\boldsymbol{u}| = 1$, the l^2-norm of G_θ is proportional to the thermal dissipation rate ϵ_T, i.e. $|\mathsf{G}_\theta|^2 = |\nabla T|^2 = (RaPr)^{1/2}\epsilon_T$. Moreover, the viscous and thermal dissipation rates are found to be locally interacted in the regions of thermal plumes, in particular when they

exceed their mean values, as outlined in Dabbagh *et al.*[28]. Consequently, it seems appropriate to utilize the tensor G_θ in order to investigate that important mechanism of turbulent heat transport (plumes) in a small scale point-of-view. To do so, we analyse the fine-scale dynamics deeply coupled with the evolution of the thermal plumes by considering a similar approach as for the classical tensor G, applied on the basic invariants of the traceless part of the new tensor, meaning $\tilde{\mathsf{G}}_\theta = \mathsf{G}_\theta - 1/3tr(\mathsf{G}_\theta)\mathsf{I}$. This can permit the analysing of the tensor characteristics identically to the G tensor.

As a starting point, we introduce the evolution equation for $\boldsymbol{u}T$ that follows from the NS and the energy equations (Eqs.1 and 2) through the formula $D(\boldsymbol{u}T)/Dt = \boldsymbol{u}DT/Dt + TD\boldsymbol{u}/Dt$, as:

$$\frac{D(\boldsymbol{u}T)}{Dt} = T(\boldsymbol{f} - \nabla p) + \sqrt{\frac{Pr}{Ra}}T\nabla^2\boldsymbol{u} + \frac{1}{\sqrt{RaPr}}\boldsymbol{u}\nabla^2 T. \tag{19}$$

At this point, the essential ideas behind this equation can be conveyed more easily by assuming that $Pr = 1$. In this case, the evolution equation reads:

$$\frac{D(\boldsymbol{u}T)}{Dt} = T(\boldsymbol{f} - \nabla p) + \frac{1}{\sqrt{Ra}}\left(\nabla^2(\boldsymbol{u}T) - 2\nabla\boldsymbol{u}\cdot\nabla T\right). \tag{20}$$

Similarly to the kinetic energy transport equation $|\boldsymbol{u}|^2/2$, the evolution equation of $e_T = |\boldsymbol{u}T|^2/2$ is introduced as:

$$\frac{De_T}{Dt} = \boldsymbol{u}T^2\cdot(\boldsymbol{f} - \nabla p) + \frac{1}{\sqrt{Ra}}\left(\nabla^2 e_T - \nabla(\boldsymbol{u}T):\nabla(\boldsymbol{u}T) - 2\boldsymbol{u}T\cdot\nabla\boldsymbol{u}\cdot\nabla T\right). \tag{21}$$

Notice that the l^2-norm of G_θ contributes to the diffusive term of e_T evolution equation, *i.e.* $\nabla(\boldsymbol{u}T):\nabla(\boldsymbol{u}T) = \mathsf{G}_\theta:\mathsf{G}_\theta = |\mathsf{G}_\theta|^2$. This characterizes the action of thermal plumes in dissipating the heat flux and feeding the momentum. In other words, high values of $|\mathsf{G}_\theta|$ differentiate zones of high gradient heat flux from the rest of the flow, which are deeply related with the presence of the thermal plumes. Following a determined threshold of $|\tilde{\mathsf{G}}_\theta|$, a separation criterion of the thermal plumes from the turbulent background regions (rest of the flow), can be proposed. It corresponds to the most probable heat flux dissipation, *i.e.* the value of $|\mathsf{G}_\theta|$ at which the PDF is maximal, as a consequent value of the mixing activity (the most widespread). Larger values beyond that threshold disclose deep thermal-kinetic interactions, and hence the thermal plumes, while smaller values correspond to the turbulent background, as visually clear in Figure 12.

(a)
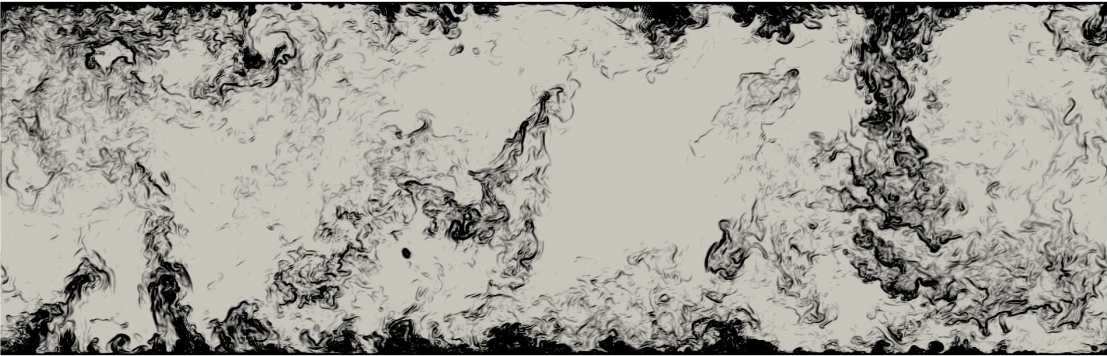
(b)

FIG. 12: Visualization of the thermal plumes (black color) in (x, z) plane, indicated by high values of $|\tilde{\mathsf{G}}_\theta|$, past specific thresholds read $|\tilde{\mathsf{G}}_\theta| > 0.214$ for $Ra = 10^8$ in (a) and $|\tilde{\mathsf{G}}_\theta| > 0.154$ for $Ra = 10^{10}$ in (b). (See movies of plumes separation MULTIMEDIA VIEW)

The invariant $Q_{\tilde{\mathsf{G}}_\theta} = -1/2 tr(\tilde{\mathsf{G}}_\theta^2)$, has a similar meaning as $|\tilde{\mathsf{G}}_\theta|$ in describing the intensity of gradient heat flux. It visualizes the (fine-scale) structures associated with high kinetic-thermal interactions. Its highest positive and negative values indicate the relevant thermal structures, while the near zero ones correspond to the turbulent background and well-mixing zones. As shown in Figure 13a, one can observe how the $Q_{\tilde{\mathsf{G}}_\theta}$ structurally features the evolution of thermal plumes beyond positive and negative thresholds. Similarly $R_{\tilde{\mathsf{G}}_\theta} = -1/3 tr(\tilde{\mathsf{G}}_\theta^3)$, is introduced as a third moment of concentrated kinetic-thermal small scale interactions. It nearly obeys a similar distribution to the skewness profile of the temperature fluctuation calculated by Emran and Schumacher[43], as shown in Figure 13b. Therein, the profiles of $\langle Q_{\tilde{\mathsf{G}}_\theta}/\langle Q_{\tilde{\Omega}_\theta}\rangle\rangle_A$ and $\langle R_{\tilde{\mathsf{G}}_\theta}/\langle Q_{\tilde{\Omega}_\theta}\rangle^{3/2}\rangle_A$ have been plotted in the lower turbulent case, since the better determination of thermals always belongs to $Ra = 10^8$ in
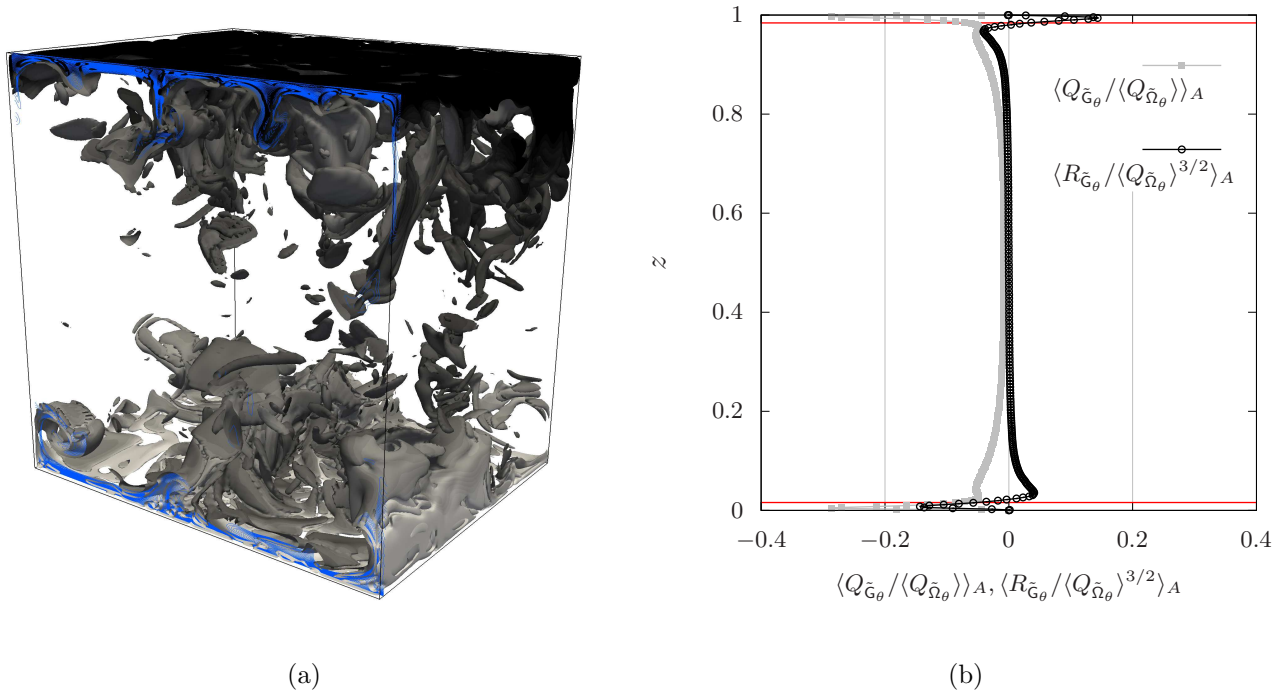
29

(a)   (b)

FIG. 13: (a) structures of high positive and negative values of $Q_{\tilde{\mathsf{G}}_\theta}$ $(-0.7143 > Q_{\tilde{\mathsf{G}}_\theta} > 0.7143)$
figured through a portion of the domain at $Ra = 10^8$ (See movies of their dynamics
MULTIMEDIA VIEW), where the blue contours indicate the hot and cold plumes. (b) represents
the averaged temporal and spatial (x-y) profiles of normalized invariants $Q_{\tilde{\mathsf{G}}_\theta}$ and $R_{\tilde{\mathsf{G}}_\theta}$ along the
z distance, where the solid red lines refer to δ_T

.

this study. Briefly speaking from Figure 13b, the two profiles of invariants start from zero
value at the isothermal walls towards negative averaged values of $Q_{\tilde{\mathsf{G}}_\theta}$ within the thermal
BLs. However, $R_{\tilde{\mathsf{G}}_\theta}$ tends to have negative and positive values through the BLs in corre-
spondence with the moving up and down thermals (plumes). Afterwards, in the bulk both
mean invariants hold a zero value due to the mixing action and plumes diffusion.

A.   Joint PDF of invariants $Q_{\tilde{\mathsf{G}}_\theta}$ and $R_{\tilde{\mathsf{G}}_\theta}$

Likewise in the classical tensor, the qualitative properties of the new invariants $Q_{\tilde{\mathsf{G}}_\theta}$ and
$R_{\tilde{\mathsf{G}}_\theta}$ are investigated by means of plotting their joint PDF, as represented in Figure 14.

30

The statistical analysis therein is similar to the classical-based one reported in Figure 5, except that the studied regime is extended broadly to cover all the domain in order to include the vicinities of emanating thermals. Interestingly, the general aspect shown in Figures 14a and 14b tends to be symmetric respect to $R_{\tilde{\mathsf{G}}_\theta} = 0$. Thereby, it seems to follow the statistical characteristics of the thermal plumes since various studies have revealed the log-normal statistics as a universal distribution for the thermal plumes geometries. For example, Zhou and Xia[45] showed that the sizes of the mushroom-like plumes obey log-normal statistics. Likewise, the geometric measures of the sheet-like plumes such as its normalized area, length and width, its aspect ratio and the shape complexity[44], as well the heat content[46], are all log-normally distributed.

From observing the statistics in Figure 14, one can note how the distributions in both cases obey an arrangement similar to the isolines of discriminant $D_{\tilde{\mathsf{G}}_\theta} = (27/4)R_{\tilde{\mathsf{G}}_\theta}^2 + Q_{\tilde{\mathsf{G}}_\theta}^3$, drawn in the $(Q_{\tilde{\mathsf{G}}_\theta}, R_{\tilde{\mathsf{G}}_\theta})$ space (Figure 14c). By definition, the discriminant holds a similar significance as $Q_{\tilde{\mathsf{G}}_\theta}$ and $R_{\tilde{\mathsf{G}}_\theta}$ invariants, since it formulates their combination to follow identically the regions tightly associated with the thermal plumes. Particularly in the hard turbulent state (Figure 14b), when the plumes are evolving in many scaled-down fragments, the statistics shows a clear following to $D_{\tilde{\mathsf{G}}_\theta}$-isolines due to the extensive amount of plumes generated. In a general description, both cases share the aspect that most of the flow is occupied by well-mixed areas (turbulent background) of very low $(Q_{\tilde{\mathsf{G}}_\theta}, R_{\tilde{\mathsf{G}}_\theta})$ values near the origin, while the thermal plumes take high values (negative and positive) of invariants far from the origin. The plumes at $Ra = 10^8$ are identified in relatively large geometries, emanate few and elongate significantly into the bulk (mushroom-like) before scattering. Therefore, the points in Figure 14a become more dispersed to take relatively high values of $(Q_{\tilde{\mathsf{G}}_\theta}, R_{\tilde{\mathsf{G}}_\theta})$. They compose a joint PDF feature which seems to be almost similar to the one based on a Gaussian flow field (see Tsinober[2] Figure 9.1(f) as an example of joint PDF of $(Q_\mathsf{G}, R_\mathsf{G})$ for a Gaussian velocity field). However, in the hard turbulent state, the plumes are abundantly emitted in the BLs, and rapidly destroyed in the bulk to make the points closely located next to the origin, holding moderate values of $(Q_\mathsf{G}, R_\mathsf{G})$ (Figure 16b). Since the mean profile of $Q_{\tilde{\mathsf{G}}_\theta}$, displayed in Figure 13b, appears to be negatively shifted inside the thermal BLs, it suggests that most of the plumes (sheet-like) or the deep kinetic-thermal interactions therein, are indicated by $Q_{\tilde{\mathsf{G}}_\theta} < 0$ values. Hence, many more points are placed down under the line $D_{\tilde{\mathsf{G}}_\theta} = 0$ in Figure 14b (than in 14a), to correspond probably with the abundant

(a)

(b)
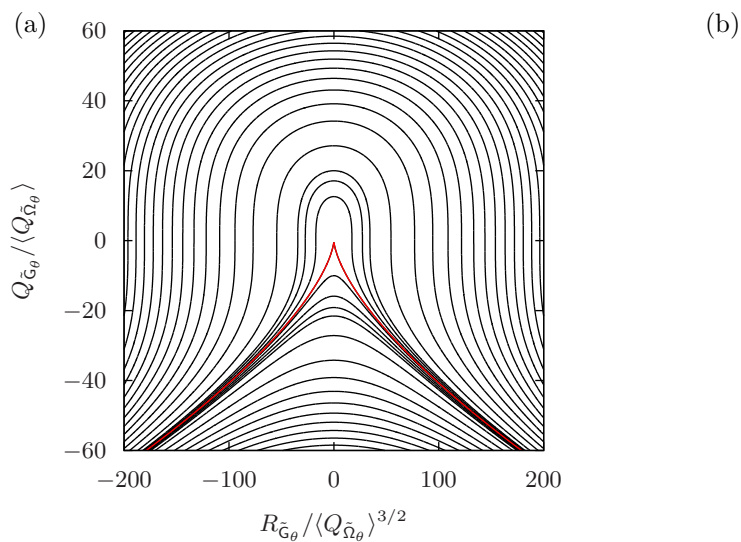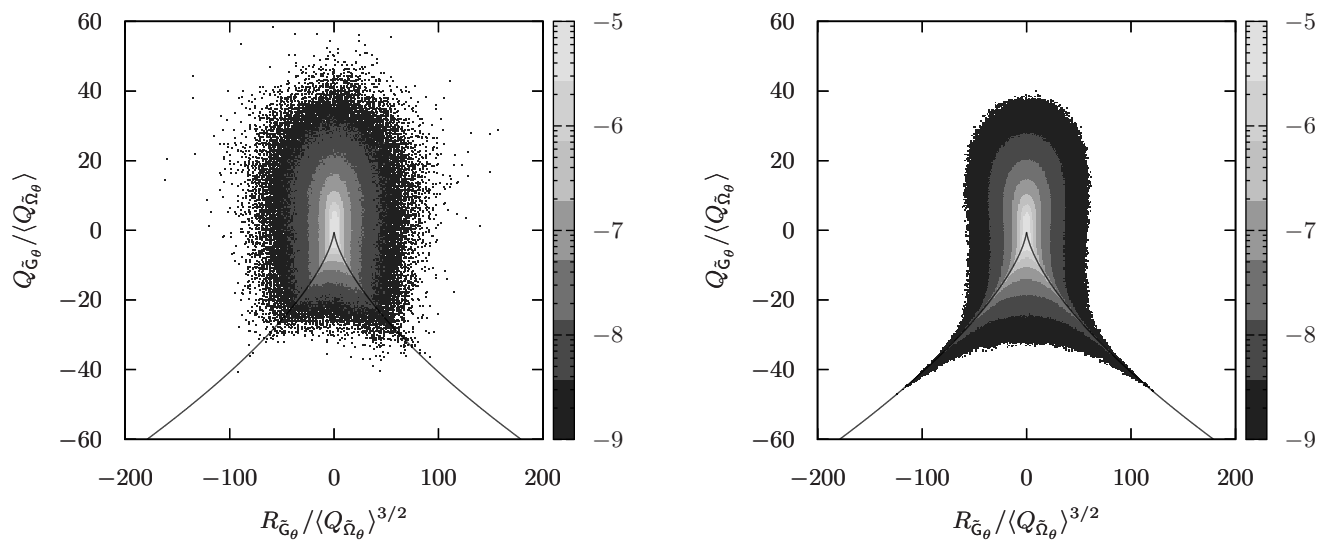
(c)

FIG. 14: Joint PDF of normalized $Q_{\tilde{\mathsf{G}}_\theta}$ and $R_{\tilde{\mathsf{G}}_\theta}$ on logarithmic scale at (a) $Ra = 10^8$ and (b) $Ra = 10^{10}$, in the whole domain. (c) displays the representative isolines of the discriminant $D_{\tilde{\mathsf{G}}_\theta} = (27/4)R_{\tilde{\mathsf{G}}_\theta}^2 + Q_{\tilde{\mathsf{G}}_\theta}^3$ in the invariants space, where the solid tent-black line in (a), (b) and the red identical one in (c), is $D_{\tilde{\mathsf{G}}_\theta} = 0$.

thermals/small-scale interactions emanating in the BLs at $Ra = 10^{10}$.

B.   Dynamics of $Q_{\tilde{\mathsf{G}}_\theta}$ and $R_{\tilde{\mathsf{G}}_\theta}$ invariants

An analysis of the dynamics of $Q_{\tilde{\mathsf{G}}_\theta}$ and $R_{\tilde{\mathsf{G}}_\theta}$ invariants, similar to the classical-based one, is considered hereafter. Firstly, the evolution equation of G_θ can be obtained easily by differentiating Eq.(20) (for such a simplified formulae considering $Pr = 1$) as follows:

$$\frac{D\mathsf{G}_\theta}{Dt} + \mathsf{G}\mathsf{G}_\theta = -\nabla T \otimes \nabla p - T\mathsf{H}(p) + 2\boldsymbol{f} \otimes \nabla T + \frac{1}{\sqrt{Ra}}\left(\nabla^2 \mathsf{G}_\theta - 2\nabla\mathsf{G} \cdot \nabla T - 2\mathsf{G}\mathsf{H}(T)\right). \quad (22)$$

Afterwards, the mean temporal rates of change in invariants $Q_{\tilde{\mathsf{G}}_\theta}$ and $R_{\tilde{\mathsf{G}}_\theta}$ have been studied in the same manner as in Section III B. They aid to elucidate the scenarios and lifetimes of the kinetic-thermal small scale motions indicating mainly the presence of the thermal plumes, their survival and their continuous mean changing under the dissipative actions. To do so, the averaging approach described in Eqs.(16) is used pertaining the new invariants $\langle DQ_{\tilde{\mathsf{G}}_\theta}/Dt\rangle, \langle DR_{\tilde{\mathsf{G}}_\theta}/Dt\rangle$, and the resultant vectors are presented together with their integral trajectories within the total domain in Figure 15. The bin size is imposed identically to obtain a division of 40×40 for the corresponding ranges of $R_{\tilde{\mathsf{G}}_\theta}/\langle Q_{\tilde{\Omega}_\theta}\rangle^{3/2}$ and $Q_{\tilde{\mathsf{G}}_\theta}/\langle Q_{\tilde{\Omega}_\theta}\rangle$, which sufficiently fulfills the convergence of the rates.

According to Figure 15, our analysis starts from the fact that the trajectories are born from zero valued $(Q_{\tilde{\mathsf{G}}_\theta}, R_{\tilde{\mathsf{G}}_\theta})$ at the isothermal walls, and move down towards the negative values of $Q_{\tilde{\mathsf{G}}_\theta}$ in correspondence with the generation of the sheet-like plumes or the roots of the original mushroom-like plumes (see Figure 16b). These roots are generated within the thermal BLs under the impact of the surrounding interaction areas, *i.e.* the impingement of the mixed flow coming from the bulk and the opposite-side plumes which reach to the BL and collide the wall therein. They excite the creation of horizontal waves (also provoked by shear strain) that travel in the BL, and interact with each other to compose the sheet-like plumes (roots). These sheet-like rods convolute and swirl away by buoyancy to arise into the bulk as the mushroom-like plumes. The areas of interactions around the roots are mostly addressed by positive values of $Q_{\tilde{\mathsf{G}}_\theta}$, as can be seen in Figure 16b. More evidence of this can be taken from the behaviour of the mean trajectories within the thermal BLs, represented in Figure 16a. Therein, the averaged evolution starts from zero to swirl downwards to

33
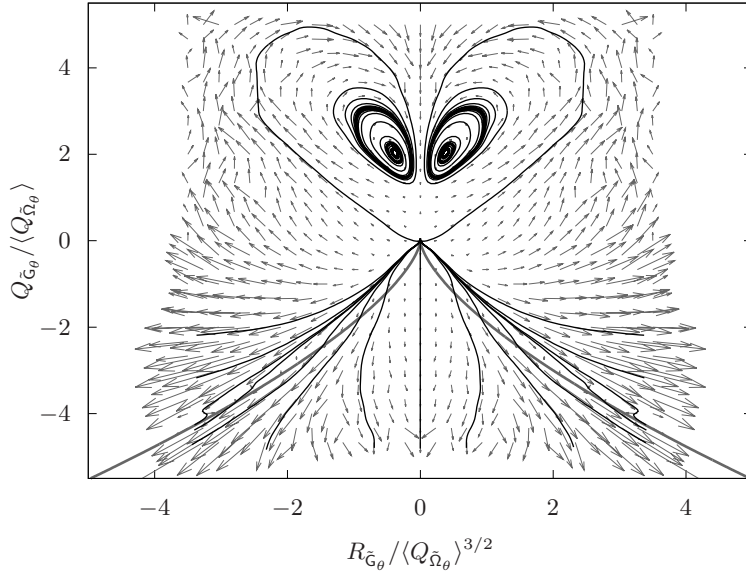
(a)
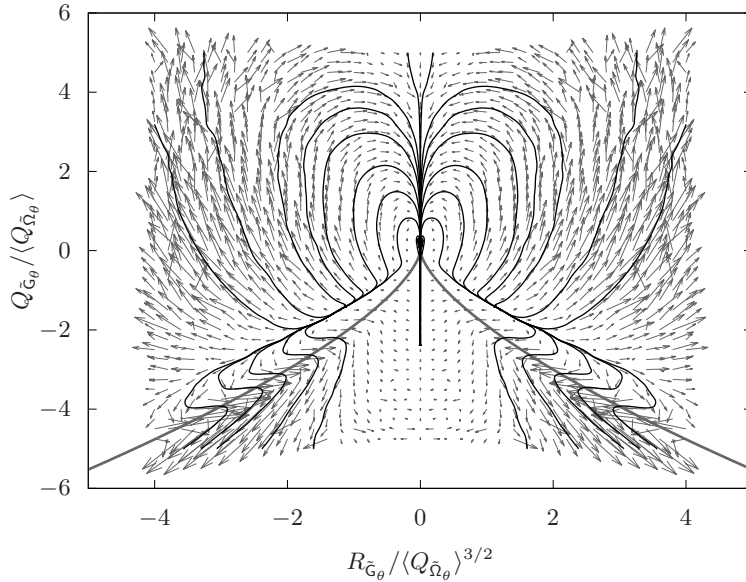
(b)

FIG. 15: Conditional mean vectors of $\langle DQ_{\tilde{\mathsf{G}}_\theta}/Dt \rangle, \langle DR_{\tilde{\mathsf{G}}_\theta}/Dt \rangle$ in $(Q_{\tilde{\mathsf{G}}_\theta}, R_{\tilde{\mathsf{G}}_\theta})$ plane together with their integral trajectories (black solid orbits) at (a) $Ra = 10^8$ and (b) $Ra = 10^{10}$, through the total domain, where the bold solid line indicates $D_{\tilde{\mathsf{G}}_\theta} = 0$.

$Q_{\tilde{\mathsf{G}}_\theta} < 0$ from $R_{\tilde{\mathsf{G}}_\theta} > 0$ to $R_{\tilde{\mathsf{G}}_\theta} < 0$ in the hot BL, and conversely in the cold one. This action accordingly validates the behaviour of $Q_{\tilde{\mathsf{G}}_\theta}$ and $R_{\tilde{\mathsf{G}}_\theta}$ mean profiles showed in Figure 13b to

34

emphasize correctly on their aforementioned meanings.

Going back to Figure 15 and along the downward path, the mean rates of invariants are slowing down with directional change at crossing the null-discriminant curve to later continue moving separately upwards away or downwards asymptotically parallel to the null-discriminant curve. This slowdown could be returned to the fact that no plumes formulation exists in that zone as $D_{\tilde{G}_\theta}$ analogously follows the evolution of plumes. However, from a physical point of view, it can give us an impression that the curve of null-discriminant can separate the sheet-like plumes evolution that moves downwards, from the evolution of the arisen mushroom-like plumes which moves upwards. The phenomenon of the directional change in the harder turbulent state is so remarkable because of the extreme emanating plumes in general, and many provoked sheet-like plumes attend to favourable fluctuations and intermittency within the BL.

All the trajectories tend to move rapidly towards high positive and negative values of $(Q_{\tilde{G}_\theta}, R_{\tilde{G}_\theta})$, to eventually address the fine-scale relevant dynamics of thermal plumes. Above the curve $D_{\tilde{G}_\theta} = 0$, the trajectories reveal an upward spiraling behaviour before converging towards two skew-symmetric origins in respect to $R_{\tilde{G}_\theta} = 0$ (mostly referring to the hot and cold thermals) at $Ra = 10^8$ (see Figure 15a). The trajectories near origins probably indicate the mean evolution and lifecycle of the mushroom-like thermal plumes that elongate far from the thermal BLs and contribute predominately to the coherent large scales of heat flux. By measuring the period of one periodic orbit around the origin (the bigger orbits), we see that it follows the lifetime of plumes $\tilde{T}_0 = 6.56 \sim 3\tau_{pl} = 6.58 [TU]$, since the plumes travel mostly in groups near the lateral sidewalls and organize to the large-scale circulation therebeside. In the hard turbulent state addressed in Figure 15b, the spiraling trajectories seem to travel upwards in shorter tracks (than in $Ra = 10^8$) to show the reduced lifetime of the mushroom-like plumes under the dissipative and mixing effects. The flow regime, at $Ra = 10^{10}$, is essentially characterized by high perturbations and a noteworthy local self-amplification of velocity derivatives $-Q_S$. The plumes are abundantly emitted in the BLs as scaled-down fragments. They scatter effectively under the impact of the amplified mixing $(-Q_S)$ to eventually make the trajectories converging towards a zero-valued origin (Figure 15b). This accordingly, suggests that the thermal plumes, at the high Ra number, do not contribute
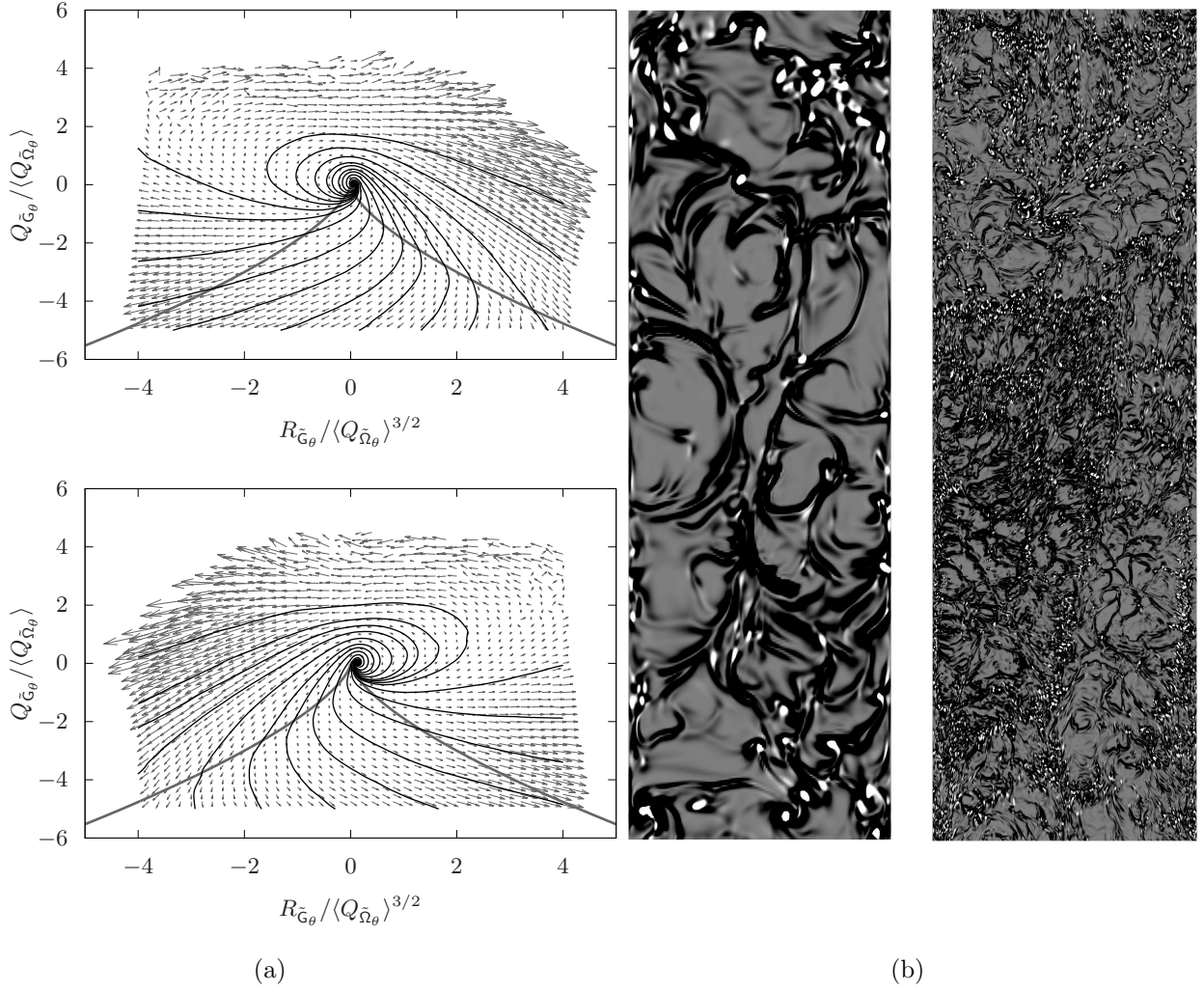
FIG. 16: (a) represents the same approach as displayed in Figure 15, but calculated within the thermal hot (top) and cold (bottom) boundary layers at $Ra = 10^{10}$. (b) shows horizontal (x, y) planes of high positive (white) and negative (black) values of $Q_{\tilde{G}_\theta}$ extracted at the hot thermal BL levels $z = 0.016$ for $Ra = 10^8$ (left), and $z = 0.004$ for $Ra = 10^{10}$ (right).

to the mean large scales of heat flux, and just give them a life. This in turn, is not so strange since experiments and DNS indicate that the large scale circulation decreases with increasing the Ra which can be attributed to the decreasing fragmentation of the plumes[14].

In order to give a broader picture, the mean rate trajectories of $Q_{\tilde{G}_\theta}$ and $R_{\tilde{G}_\theta}$ invariants are plotted similarly, through the bulk region (V_{bulk}) in Figure 17a. Therein, all the trajectories obey generally an upward moving action decaying towards a zero-valued origins for both
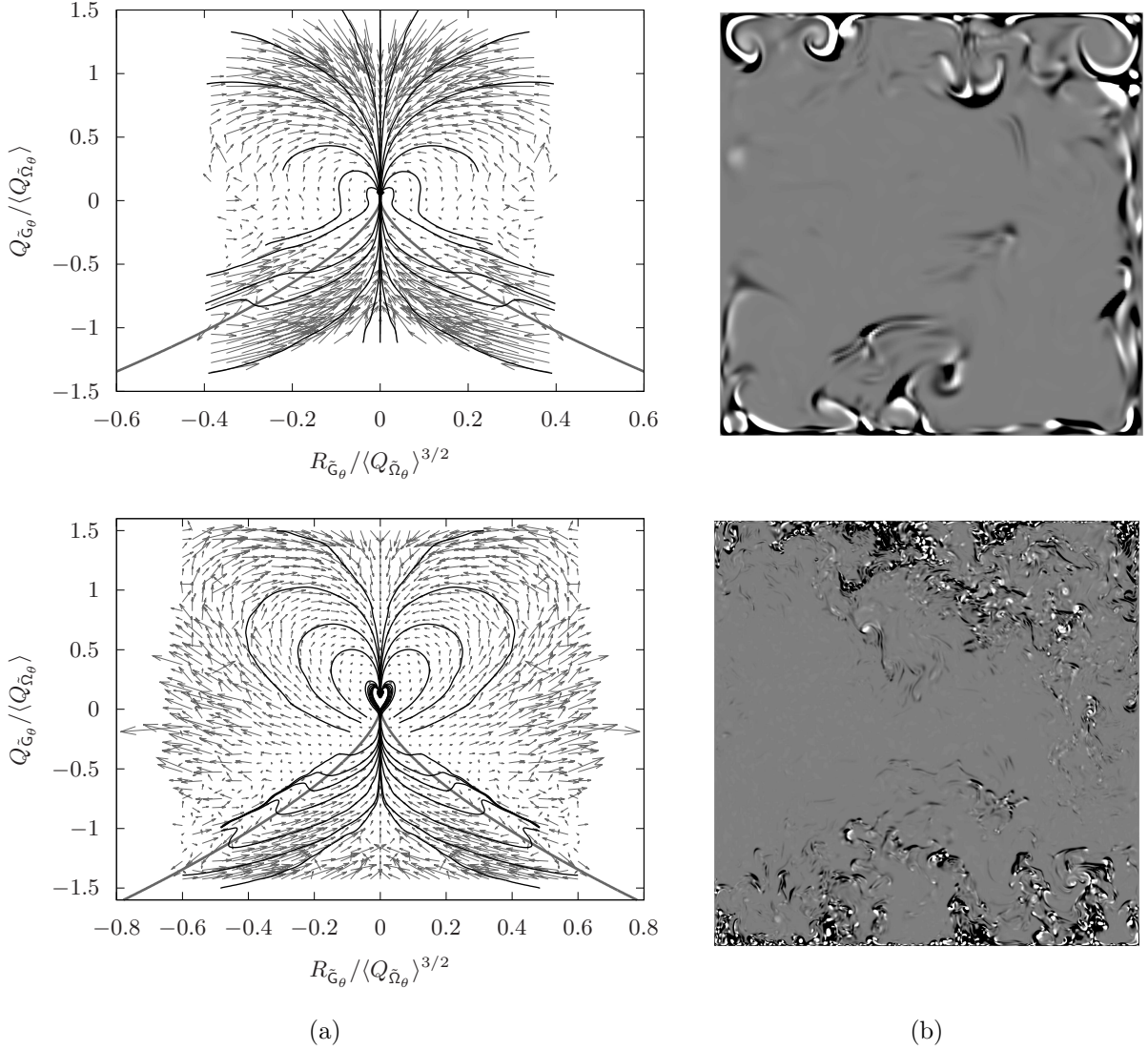
FIG. 17: (a) the same representations as Figure 15, but through the bulk region (V_{bulk}), for $Ra = 10^8$ (top) and $Ra = 10^{10}$ (bottom). (b) displays vertical planes (y, z) of $Q_{\tilde{\mathsf{G}}_\theta}$ coloured similarly to Figure 16b, for $Ra = 10^8$ (top) and $Ra = 10^{10}$ (bottom).

Ra numbers. Below the $D_{\tilde{\mathsf{G}}_\theta} = 0$ curve, the mean rate tracks are moving up indicating the extended parts of the original plumes in the bulk. Likewise, above the null-discriminant curve the tracks are upwarded in spiraling behaviour to address the elongating action of the mushroom-like plumes, and the subsequent scattering by the dissipative mixing (see Figure 17b). It can be an interesting point observing the upward direction behaviour of the tracks in region of $Q_{\tilde{\mathsf{G}}_\theta} < 0$ through the bulk, whereas they were downwarded in the whole domain (Figure 15). This manifests the fact that two evolutions of plumes exist: the sheet-

37

like ones or the original roots that emanate in the BLs, and the the mushroom-like ones, which travel and expand in the bulk. It is also worthwhile noting that the trajectories swirl with longer and wider tracks above the $D_{\tilde{\mathsf{G}}_\theta} = 0$ curve in Figure 17b (than in Figure 17a). This can be classified as a natural result of increasing the rate of plumes production, injected forwards in the bulk, at $Ra = 10^{10}$. Finally, in both cases, all the trajectories seem to converge towards zero-value origins due to the effective mixing activities in the bulk, keeping in mind that V_{bulk} is quite far of including the solid wall influences. The plumes are destroyed in mean, absolutely at a constant averaged heat flux across the bulk, and yielding naturally to a zero-gradient heat flux and null means for $Q_{\tilde{\mathsf{G}}_\theta}$ and $R_{\tilde{\mathsf{G}}_\theta}$ (see Figure 13b).

V.   CONCLUDING REMARKS AND FUTURE RESEARCH

Several universal small-scale features observed in various turbulent flows have been re-captured in buoyancy-driven turbulent RBC. Two turbulent cases at Ra-numbers 10^8 and 10^{10}, within an air-filled rectangular cell of aspect ratio unity and π span-wise open-ended distance, are considered in a DNS study. The universal inclined "teardrop" shape of the joint PDF statistics of the classical invariants $(Q_{\mathsf{G}}, R_{\mathsf{G}})$ through the bulk region are observed. Furthermore, the mean temporal rate of invariants change $(\langle DQ_{\mathsf{G}}/Dt \rangle, \langle DR_{\mathsf{G}}/Dt \rangle)$ is plotted in that region to reveal the common spiralling clockwise behaviour of trajectories converging towards the origin. In consistency with previous studies on the small-scale motions (Ooi *et al.*[5] and Elsinga and Marusic[6]), the topology surrounding a fluid particle is varying in a cyclical aspect, in the $(Q_{\mathsf{G}}, R_{\mathsf{G}})$ space, from unstable focus, unstable node, stable node to stable focus structures in the both cases. A local self-amplification of velocity derivatives (viscous straining $-Q_{\mathsf{S}}$ in the turbulent background) at $Ra = 10^{10}$, aids in contracting the vorticity worms further which assists the decaying events (interplay of the non-local pressure Hessian with the viscous diffusion and energy-injecting terms), and bends the trajectories inwards above the null-discriminant curve. The one period of the periodic spiral orbits near the origin is found to approach $T_0 \sim \tau_{eddy}$ an estimated large eddy turnover time defined in the bulk. On the other hand, the measured period has been compared with the average plume lifetime $T_0 \sim 3\tau_{pl}$ to suggest the participation of the thermal plumes in the large-scale kinetic energy containing eddies and turbulent wind created in the bulk; particularly when the plumes elongate significantly before scattering, at

$Ra = 10^8$. Other universal features of (small scale) 3D turbulence are observed through the bulk region. For example, the preferential alignment between $\boldsymbol{\omega}$ and $\boldsymbol{\lambda}_2$ the intermediate eigenstrain vector, and the asymmetric $\boldsymbol{\omega}$ alignment with the vortex-stretching vector. The local self-amplification of velocity derivatives $(-Q_{\mathsf{S}}/Q_{\Omega})$ at $Ra = 10^{10}$ has revealed enhanced local effects associated with (self) interactions of vorticity/strain in the strain dominated regions and thus, improve slightly the linear contributions of the vortex stretching mechanism.

On the other hand, the evolution of relevant thermals has been addressed in small scale point-of-views. Namely, considering the invariants of the traceless part of velocity-times-temperature gradient tensor $(Q_{\tilde{\mathsf{G}}_\theta}, R_{\tilde{\mathsf{G}}_\theta})$, an identical approach of studying their mean temporal rate and joint PDF, has been applied. The new invariants have demonstrated a direct picture on the small-scale kinetic and thermal interaction dynamics. They have expressed a correct following to the evolution of thermal plumes in RBC. It is found that the conditional averaged trajectories travel downwards to expose the sheet-like plumes dynamics (roots) within the BLs, and upwards to exhibit the mushroom-like plumes evolution that expand in the bulk. The trajectories –through the total domain– spiral upwards before converging towards two skew-symmetric origins with periodic orbits correspond in their period to approximately 3 times the lifetime of plumes at $Ra = 10^8$. By that end, it was emphasized on the predominant role of hot and cold plumes in contributing to the coherent large scales of heat flux, in average, which roll near the lateral sidewalls. Shorter tracks of the trajectories have been recorded at the higher Ra number (in the whole domain) to show the reduced lifetime of mushroom-like plumes under the dissipative and mixing effects. At that Ra, the flow regime is essentially characterized by high perturbations and a noteworthy local self-amplification of velocity derivatives $-Q_{\mathsf{S}}$. It exceeds the evolution of thermal plumes, which emanate abundantly in small-scale geometries, in the BL. The plumes scatter strongly under the amplified turbulent background mixing events to make the trajectories converging towards a zero-valued origin. This accordingly has suggested that the thermal plumes at this high Ra number do not contribute to the mean large scales of heat flux and just give them a life. Finally, and due to the effective mixing activities, all the averaged trajectories through the bulk have revealed an upwards movement (mushroom-like plumes) decaying towards a zero-valued origins for both Ra numbers, since the heat flux is constant spatially and temporally in mean and the plumes are completely destroyed with zero-valued

means of $Q_{\tilde{\mathsf{G}}_\theta}$ and $R_{\tilde{\mathsf{G}}_\theta}$.

In summary, these findings have extended the scope of small-scale turbulence universality to include the turbulent buoyancy-driven flows. On the other hand, the observations of $Q_{\tilde{\mathsf{G}}_\theta}$ and $R_{\tilde{\mathsf{G}}_\theta}$ invariants behaviour have demonstrated a successful prediction to the mean evolution of the small scale motions associated intrinsically with the thermal plumes, which can open many options in turbulence modeling approaches of thermals. This will be an essential topic in our future research plans.

ACKNOWLEDGMENTS

REFERENCES

[1] R. H. Kraichnan. Some modern developments in the statistical theory of turbulence. Statistical mechanics: New concepts, New Problems, New Applications. pages 201–228. The University of Chicago Press, 1972.

[2] A Tsinober. *An Informal Introduction to Turbulence*, volume **63**. Fluid Mechanics and its Applications, Kluwer Academic Publishers, 2001.

[3] M. S. Chong, A. E. Perry, and B. J. Cantwell. A general classification of three-dimensional flow fields. *Physics of Fluids A*, **2**:765, 1990.

[4] J. Martín, A. Ooi, M. S. Chong, and J. Soria. Dynamics of the velocity gradient tensor invariants in isotropic turbulence. *Physics of Fluids*, **10**:2336, 1998.

[5] A. Ooi, J. Martin, J. Soria, and M. S. Chong. A study of the evolution and characteristics of the invariants of the velocity-gradient tensor in isotropic turbulence. *Journal of Fluid Mechanics*, **381**:141, 1999.

[6] G. E. Elsinga and I. Marusic. Evolution and lifetimes of flow topology in a turbulent boundary layer. *Physics of Fluids*, **22**(1):015102, 2010.

[7] H. M. Blackburn, N. N. Mansour, and B. J. Cantwell. Topology of fine-scale motions in turbulent channel flow. *Journal of Fluid Mechanics*, **310**:269–292, 1996.

[8] J. Soria, R. Sondergaard, B. J. Cantwell, M. S. Chong, and A. E. Perry. A study of the fine-scale motions of incompressible time-developing mixing layers. *Physics of Fluids*, **6**(2):871–884, 1994.

[9] C. B. da Silva and J. C. F. Pereira. Invariants of the velocity-gradient, rate-of-strain, and rate-of-rotation tensors across the turbulent/nonturbulent interface in jets. *Physics of Fluids*, **20**(5):055101, 2008.

[10] S. Park and C. Lee. Analysis of coherent structures in Rayleigh-Bénard convection. *Journal of Turbulence*, **16**(12):1162–1178, 2015.

[11] K. Hanjalić. One-point closure models for buoyancy-driven turbulent flows. *Annual Reviews of Fluid Mechanics*, **34**:321–347, 2002.

[12] E. D. Sigga. High Rayleigh number convection. *Annual Reviews of Fluid Mechanics*, **26**:137, 1994.

[13] S. Grossmann and D. Lohse. Fluctuations in turbulent Rayleigh-Bénard convection: The role of plumes. *Physics of Fluids*, **1**:4462–4472, 2004.

[14] F. Chillà and J. Schumacher. New perspectives in turbulent Rayleigh-Bénard convection. *The European Physics Journal E*, **35**:58, 2012.

[15] D. Lohse and K. Xia. Small-scale properties of turbulent Rayleigh-Bénard convection. *Annual Reviews of Fluid Mechanics*, **42**:335–364, 2010.

[16] J. Schumacher. Lagrangian dispersion and heat transport in convective turbulence. *Physical Review Letters*, **100**:134502, 2008.

[17] Y. Gasteuil, WL. Shew, M. Gilber, F. Chillà, B. Castaing, and JF. Pinton. Lagrangian temperature, velocity, and local heat flux measurement in Rayleigh-Bénard convection. *Physical Review Letters*, **99**:234302, 2007.

[18] J. Scheel, M. S. Emran, and J. Schumacher. Resolving the fine-scale structure in turbulent Rayleigh-Bénard convection. *New Journal of Physics*, **15**:113063, 2013.

[19] M. Kaczorowski and K. Xia. Turbulent flow in the bulk of Rayleigh-Bénard convection: small-scale properties in a cubic cell. *Journal of Fluid Mechanics*, **722**:596–617, 2013.

[20] J. Schumacher, J. D. Scheel, D. Krasnov, D. A. Donzis, V. Yakhot, and K. R. Sreeni-

vasan. Small-scale universality in fluid turbulence. *Proceedings of the National Academy of Sciences*, **111**(30):10961–10965, 2014.

[21]R. W. C. P. Verstappen and A. E. P. Veldman. Symmetry-preserving discretization of turbulent flow. *Journal of Computational Physics*, **187**:343–368, 2003.

[22]F. X. Trias and O. Lehmkuhl. A self-adaptive strategy for the time-integration of Navier-Stokes equations. *Numerical Heat Transfer, part B*, **60**(2):116–134, 2011.

[23]A. J. Chorin. Numerical solution of the Navier-Stokes equation. *Mathematics of Computation*, **22**:745–762, 1968.

[24]A. Gorobets, F. X. Trias, and A. Oliva. A parallel MPI+OpenMP+OpenCL algorithm for hybrid supercomputations of incompressible flows. *Computers and Fluids*, **88**:764–772, 2013.

[25]F. X. Trias, M. Soria, C. D. Pérez-Segarra, and A. Oliva. Direct numerical simulation of two- and three-dimensional turbulent natural convection flows in a differentially heated cavity of aspect ratio 4. *Journal of Fluid Mechanics*, **586**:259–293, 2007.

[26]R. A. J. M. Stevens, R. Verzicco, and D. Lohse. Radial boundary layer structure and Nusselt number in Rayleigh-Bénard convection. *Journal of Fluid Mechanics*, **643**:495–507, 2010.

[27]G. Grötzbach. Spatial resolution requirements for direct numerical simulation of the Rayleigh-Bénard convection. *Journal of Computational Physics*, **49**:241–264, 1983.

[28]F. Dabbagh, F. X. Trias, A. Gorobets, and A. Oliva. Spectrally-consistent regularization of turbulent Rayleigh-Bénard convection. *6th European Conference on Computational Fluid Dynamics, International Center for Numerical Methods in Engineering*,pages 7144–7155, 2014.

[29]O. Shishkina, R. J. A. M. Stevens, S. Grossmann, and D. Lohse. Boundary layer structure in structure in turbulent thermal convection and consequences for the required numerical resolution. *New Journal of Physics*, **12**:075022, 2010.

[30]M. Van Reeuwijk, H. J. J. Jonker, and K. K. Hanjalić. Identification of the wind in Rayleigh-Bénard convection. *Physics of Fluids*, **17**(5):051704, 2005.

[31]E. Brown, A. Nikolaenko, and G. Ahlers. Reorientation of the large-scale circulation in turbulent Rayleigh-Bénard convection. *Physical Review Letters*, **95**:084503, 2005.

[32]F. F. Araujo, S. Grossmann, and D. Lohse. Wind reversals in turbulent Rayleigh-Bénard convection. *Physical Review Letters*, **95**(8):084502, 2005.

[33] M. Kaczorowski and C. Wagner. Analysis of the thermal plumes in turbulent Rayleigh-Bénard convection based on well-resolved numerical simulations. *Journal of Fluid Mechanics*, **618**:89–112, 2009.

[34] J. Scheel and J. Schumacher. Local boundary layer scales in turbulent Rayleigh-Bénard convection. *Journal of Fluid Mechanics*, **758**:344–373, 2014.

[35] B. J. Cantwell. On the behavior of velocity gradient tensor invariants in direct numerical simulations of turbulence. *Physics of Fluids A*, **5**:2008, 1993.

[36] A. E. Perry and M. S. Chong. Topology of flow patterns in vortex motions and turbulence. *Applied Scientific Research*, **53**:357–374, 1994.

[37] F. X. Trias, D. Folch, A. Gorobets and A. Oliva. Building proper invariants for eddy-viscosity subgrid-scale models. *Physics of Fluids*, **27**:065103, 2015.

[38] P. E. Hamlington, J. Schumacher, and W. J. A. Dahm. Direct assessment of vorticity alignment with local and nonlocal strain rates in turbulent flows. *Physics of Fluids*, **20**:111703, 2008.

[39] B. J. Cantwell. Exact solution of the restricted Euler equation for the velocity gradient tensor. *Physics of Fluids A*, **4**:782, 1992.

[40] M. Wilczek. New insights into the fine-scale structure of turbulence. *Journal of Fluid Mechanics*, **784**:1–4, 2015.

[41] M. Kholmyansky, A. Tsinober, and S. Yorish. Velocity derivatives in the atmospheric surface layer at $Re_\lambda = 10^4$. *Physics of Fluids*, **13**:311–314, 2001.

[42] B. Lüthi, M. Holzner, and A. Tsinober. Expanding the Q-R space to three dimensions. *Journal of Fluid Mechanics*, **641**:497–507, 2009.

[43] M. S. Emran and J. Schumacher. Fine-scale statistics of temperature and its derivatives in convective turbulence. *Journal of Fluid Mechanics*, **611**:13–34, 2008.

[44] S. Q. Zhou and K. Q. Xia. Physical and geometrical properties of thermal plumes in turbulent Rayleigh-Bénard convection. *New Journal of Physics*, **12**:075006, 2010.

[45] S. Q. Zhou and K. Q. Xia. Plume statistics in thermal turbulence: mixing of an active scalar. *Physical Review Letters*, **89**:184502, 2002.

[46] S. Q. Zhou, C. Sun, and K. Q. Xia. Morphological evolution of thermal plumes in turbulent Rayleigh-Bénard convection. *Physical Review Letters*, **98**:074501, 2007.